The Peculiar Short-duration GRB 200826A and Its Supernova[*]

A. Rossi[1], B. Rothberg[2,3], E. Palazzi[1], D. A. Kann[4], P. D'Avanzo[5], L. Amati[1], S. Klose[6], A. Perego[7,8], E. Pian[1],
C. Guidorzi[1,9,10], A. S. Pozanenko[11,12,13], S. Savaglio[14], G. Stratta[1,15,16], G. Agapito[17], S. Covino[5], F. Cusano[1],
V. D'Elia[18,19], M. De Pasquale[20,21], M. Della Valle[22], O. Kuhn[2], L. Izzo[23], E. Loffredo[24,25], N. Masetti[1,26], A. Melandri[5],
P. Y. Minaev[11,12,27], A. Nicuesa Guelbenzu[6], D. Paris[19], S. Paiano[19,28,29], C. Plantet[17], F. Rossi[17], R. Salvaterra[29],
S. Schulze[30], C. Veillet[2], and A. A. Volnova[11]

[1] INAF–Osservatorio di Astrofisica e Scienza dello Spazio, via Piero Gobetti 93/3, I-40129 Bologna, Italy; andrea.rossi@inaf.it
[2] Large Binocular Telescope Observatory, University of Arizona, 933 N. Cherry Ave., Tucson, AZ 85721, USA
[3] George Mason University, Department of Physics & Astronomy, MS 3F3, 4400 University Dr., Fairfax, VA 22030, USA
[4] Instituto de Astrofísica de Andalucía (IAA-CSIC), Glorieta de la Astronomía, S/N, E-18008 Granada, Spain
[5] INAF–Osservatorio Astronomico di Brera, Via E. Bianchi 46, I-23807, Merate (LC), Italy
[6] Thüringer Landessternwarte Tautenburg, Sternwarte 5, D-07778 Tautenburg, Germany
[7] Dipartimento di Fisica, Universitá di Trento, Via Sommarive 14, I-38123 Trento, Italy
[8] INFN-TIFPA, Trento Institute for Fundamental Physics and Applications, via Sommarive 14, I-38123 Trento, Italy
[9] Department of Physics and Earth Science, University of Ferrara, via Saragat 1, I-44122, Ferrara, Italy
[10] INFN–Sezione di Ferrara, Via Saragat 1, I-44122 Ferrara, Italy
[11] Space Research Institute of the Russian Academy of Sciences (IKI), 84/32 Profsoyuznaya St., Moscow 117997, Russia
[12] Moscow Institute of Physics and Technology (MIPT), 9 Institutskiy per., Dolgoprudny, Moscow Oblast 141701, Russia
[13] National Research University Higher School of Economics, Moscow 101000, Russia
[14] Physics Department, University of Calabria, I-87036 Arcavacata di Rende, Italy
[15] INAF–Istituto di Astrofisica e Planetologia Spaziali, via Fosso del Cavaliere 100, I-00133 Roma, Italy
[16] INFN, Sezione di Roma, I-00185 Roma, Italy
[17] INAF–Osservatorio Astrofisico di Arcetri, Largo E. Fermi 5, I-50125-Firenze, Italy
[18] Space Science Data Center (SSDC)–Agenzia Spaziale Italiana (ASI), I-00133 Roma, Italy
[19] INAF–Osservatorio Astronomico di Roma, via Frascati 33, I-00040 Monte Porzio Catone, Italy
[20] University of Messina, MIFT Department, Polo Papardo, Viale F.S. D'Alcontres 31, I-98166 Messina, Italy
[21] Department of Astronomy and Space Sciences, Faculty of Science, Istanbul University, 34119 Istanbul, Turkey
[22] INAF, Osservatorio Astronomico di Capodimonte, Salita Moiariello 16, I-80131 Naples, Italy
[23] DARK, Niels Bohr Institute, University of Copenhagen, Jagtvej 128, DK-2200 Copenhagen, Denmark
[24] Gran Sasso Science Institute, Viale F. Crispi 7, I-67100, L'Aquila (AQ), Italy
[25] INFN–Laboratori Nazionali del Gran Sasso, I-67100, L'Aquila (AQ), Italy
[26] Departamento de Ciencias Físicas, Universidad Andrés Bello, Fernández Concha 700, Las Condes, Santiago, Chile
[27] P.N. Lebedev Physical Institute of the Russian Academy of Sciences, Leninskii pr. 53, Moscow, 119991, Russia
[28] INAF–Istituto di Astrofisica Spaziale e Fisica Cosmica di Palermo, via Ugo La Malfa, 153, I-90146 Palermo, Italy
[29] INAF–Istituto di Astrofisica Spaziale e Fisica Cosmica di Milano, via Alfonso Corti 12, I-20133 Milano, Italy
[30] The Oskar Klein Centre, Department of Physics, Stockholm University, Albanova University Center, SE 106 91 Stockholm, Sweden
Received 2021 May 8; revised 2022 March 14; accepted 2022 March 20; published 2022 June 8

Abstract

Gamma-ray bursts (GRBs) are classified into long and short events. Long GRBs (LGRBs) are associated with the end states of very massive stars, while short GRBs (SGRBs) are linked to the merger of compact objects. GRB 200826A was a peculiar event, because by definition it was an SGRB, with a rest-frame duration of ∼0.5 s. However, this event was energetic and soft, which is consistent with LGRBs. The relatively low redshift ($z = 0.7486$) motivated a comprehensive, multiwavelength follow-up campaign to characterize its host, search for a possible associated supernova (SN), and thus understand the origin of this burst. To this aim we obtained a combination of deep near-infrared (NIR) and optical imaging together with spectroscopy. Our analysis reveals an optical and NIR bump in the light curve whose luminosity and evolution are in agreement with several SNe associated to LGRBs. Analysis of the prompt GRB shows that this event follows the $E_{p,i}$–E_{iso} relation found for LGRBs. The host galaxy is a low-mass star-forming galaxy, typical of LGRBs, but with one of the highest star formation rates, especially with respect to its mass ($\log M_*/M_\odot = 8.6$, SFR ∼ 4.0 $M_\odot$ yr^{-1}). We conclude that GRB 200826A is a typical collapsar event in the low tail of the duration distribution of LGRBs. These findings support theoretical predictions that events produced by collapsars can be as short as 0.5 s in the host frame and further confirm that duration alone is not an efficient discriminator for the progenitor class of a GRB.

Unified Astronomy Thesaurus concepts: Gamma-ray bursts (629); Core-collapse supernovae (304); Supernovae (1668)

Supporting material: data behind figure

---

[*] Based on data obtained with the LBT programs: LBT-2019B-18 (PI A. Rossi), DDT-2019B-9 (PI P. D'Avanzo), and LD-2020B-0100 (PI. B. Rothberg); and the TNG programme A41 TAC15 (PI V. D'Elia).

1. Introduction

Traditionally, gamma-ray bursts (GRBs) are divided into two classes based on their duration and their spectral hardness in the gamma energy range. The majority of observed GRBs have durations longer than 2 s and a soft high-energy spectrum and

are termed "long GRBs" (LGRBs), as opposed to "short GRBs" (SGRBs) with a usually subsecond duration and a harder high-energy spectrum (Mazets et al. 1981; Kouveliotou et al. 1993). However, there is a substantial overlap between the distributions of the durations of the two GRB classes (Kouveliotou et al. 1993; Bromberg et al. 2013; Horváth & Tóth 2016).

LGRBs are typically associated with highly energetic broad-lined Type Ic supernovae (SNe) and have therefore been associated confidently with the deaths of very massive stars (e.g., Woosley & Bloom 2006; Cano et al. 2017a). On the other hand, SGRBs are thought to be connected with the merger of compact objects, as was firmly demonstrated in spectacular fashion by SGRB 170817A, which was accompanied by the binary neutron star (NS) merger gravitational-wave source GW170817 detected by the LIGO and Virgo interferometers as well as by the kilonova (KN) AT 2017gfo (e.g., Abbott et al. 2017a, 2017b, 2017c; Pian et al. 2017; Smartt et al. 2017).

Improving our understanding of the connection between LGRBs and SNe has been one of the most intense areas of research in the field of GRBs for over 20 years. More than 1400 bursts have been discovered by the Neil Gehrels Swift Observatory (Swift hereafter) in the last 16 years, among which only 40–50 GRBs have an associated SN identified by late bumps in their optical afterglow light curves, and to date, just 28 have been spectroscopically confirmed (A. Rossi et al. 2022, in preparation; Cano et al. 2017a; Izzo et al. 2019; Melandri et al. 2022 and references therein; Cano et al. 2017b; Ashall et al. 2019; Klose et al. 2019; Melandri et al. 2019; Hu et al. 2021). The burst duration for all these events is more than 2 s; therefore they are considered LGRBs. While these results show a simple and clear correlation between SNe and LGRBs, the reality may be more complex.

A first break in the LGRB-SN association was already found in 2006 with the discovery of LGRBs 060505 and 060614.[31] Their relatively low redshifts ($z = 0.089$ and $z = 0.125$, respectively) allowed for a search for possibly associated SNe, but despite achieving deep photometric limits no SN component as luminous as those observed in the case of other LGRBs was detected (Della Valle et al. 2006; Gal-Yam et al. 2006; Fynbo et al. 2006; Ofek et al. 2007; McBreen et al. 2008; Xu et al. 2009).[32] Later, LGRB 111005A at $z = 0.0133$ (Michałowski et al. 2018; Tanga et al. 2018) joined this group. On the other hand, in the case of GRB 040924, classified as short for its rest-frame duration (~1 s), an associated SN was detected (Soderberg et al. 2006; Wiersema et al. 2008) thus identifying its origin as the collapse of a massive star. Another peculiar case is GRB 090426, which has a duration shorter than 2 s, but has a high-energy spectrum and an afterglow brightness typical of LGRBs (Antonelli et al. 2009; Nicuesa Guelbenzu et al. 2011, 2012; Thöne et al. 2011; D. A. Kann et al. 2022, in preparation). Indeed, although classifying a burst by its duration as either long or short is still the simplest and most widely adopted approach, the above results show that this is not enough to reveal the nature of the GRB progenitor. Even considering the spectral hardness often may not help in the classification (e.g., Minaev & Pozanenko 2020a; Agüí

Fernández et al. 2021), and thus in understanding the origin of the burst. Indeed, the most secure way is to determine whether the event is associated with an SN and is an LGRB, or with a KN and is an SGRB.

We here present follow-up observations and analysis of GRB 200826A, including the search for an associated SN and characterization of the host galaxy. This very intense, but short-duration burst has been detected by several space-based GRB detectors (see Hurley et al. 2020), including Konus-Wind (Ridnaia et al. 2020; Svinkin et al. 2020), Fermi/GBM (Mangan et al. 2020), AGILE/MCAL (Pittori et al. 2020), and AstroSat/CZTI (Gupta et al. 2020). Stemming from its observed short duration (GBM $T_{90} = 1.14$ s, Mangan et al. 2020; Konus-Wind $T_{90} = 0.772$ s, Svinkin et al. 2020), it was initially thought to be a genuine SGRB. The Zwicky Transient Facility (ZTF) survey project (Bellm et al. 2019) launched an observing campaign to search for the optical counterpart (Sagues Carracedo et al. 2020) within the large error circle of Fermi/GBM. Among the several candidates detected, ZTF 20abwysqy was confirmed to be the afterglow of GRB 200826A (Ahumada et al. 2020a; Belkin et al. 2020a; Dichiara et al. 2020). An X-ray afterglow was also detected by Swift/XRT (D'Ai et al. 2020). The GRB spectroscopic redshift ($z = 0.748$) was obtained thanks to LBT/MODS observations (Rothberg et al. 2020a). The provided distance was used to calculate the real luminosities and energy values, which showed that GRB 200826A was a very energetic event with an isotropic energy release and a peak energy more consistent with classical LGRBs than with typical SGRBs (Svinkin et al. 2020). An SN bump in the afterglow light curve was finally reported by Ahumada et al. (2020c). Additional optical observations of the afterglow and the SN have been reported in Ahumada et al. (2021) and Zhang et al. (2021).

Throughout this work, the flux density of the afterglow is described as $F_\nu(t) \propto t^{-\alpha}\nu^{-\beta}$, and a ΛCDM world model with $\Omega_M = 0.308$, $\Omega_\Lambda = 0.692$, and $H_0 = 67.8$ km s^{-1} Mpc^{-1} (Planck Collaboration et al. 2016) is assumed. All data are in the observer frame, unless otherwise specified.

2. Observations and Data Analysis

2.1. Optical Spectroscopy

Optical spectroscopy of GRB 200826A was obtained with the Large Binocular Telescope (LBT) on Mount Graham, Arizona, USA, on 2020 August 28, at UT 09:06:45 (MJD 59,089.379692) using both optical Multi-object Double Spectrographs (MODS; Pogge et al. 2010). Each of the MODS was configured using a 1″ wide slit ($R \sim 1500$). MODS1 was configured with the red grating (0.58 μm–1.0 μm coverage) due to issues at the time with the blue channel, and MODS2 was configured with the dual grating (0.32 μm–1.05 μm coverage). Observations consisted of 4×900 s exposures for the three channels, which yielded an effective exposure time of 7200 s for 0.58 μm-1.0 μm (the red channels). A position angle = 17°.0 was used in order to cover both the reported location of the GRB 200826A afterglow and a nearby galaxy 15″ NE. Observations were obtained at or near transit with an effective airmass of 1.0005. The seeing for the spectroscopic observations ranged from 0″.7 to 1″.0 and the sky conditions were photometric.

The MODS data were reduced first with modsCCDRed version 2.04 to remove bias and flat-field the data. Next,

---

[31] GRBs 060505 and 060614 have durations (T_{90}) of 4 ± 1 s (Hullinger et al. 2006) and $\sim 102 \pm 5$ s (Barthelmy et al. 2006), respectively.

[32] More recently, KNe have been claimed to have been detected in the afterglows of GRB 060614 (Jin et al. 2015; Yang et al. 2015) and GRB 060505 (Jin et al. 2021). This would imply they are actually merger events (see Kann et al. 2011 for more discussion).

custom IRAF scripts were used to extract along the central slit using a stellar trace, wavelength-calibrate and rectify the tilt in both the X and Y directions using arc-lamp lines, flux-calibrate the data using the spectrophotometric standard star G191-B2B, and remove telluric features from the red channels using the spectrophotometric standard. The data from the three channels were combined into a single spectrum and rebinned to a common scale of $\Delta\lambda = 0.85$ Å pixel^{-1}. The afterglow spectral energy distribution (SED) (Section 3) was then subtracted from the spectrum and the absolute flux calibration was fine-tuned using the late-time g', r', i', and z' MODS and Large Binocular Cameras (LBC; Giallongo et al. 2008) photometry (Table 1), which is free from SN and afterglow emission (see Section 2.4).

2.2. Optical and Near-infrared Imaging

Optical follow-up was performed with the LBT in the Sloan filter g' and r' bands using the twin MODS instruments, and in the Sloan r' filter with the Device Optimized for the Low Resolution (DOLoRes) optical imager and spectrograph mounted on Telescopio Nazionale Galileo (TNG) in La Palma (Canary Islands, Spain). We also observed GRB 200826A twice with the AZT-22 1.5 m telescope equipped with a SNUCAM CCD camera (Im et al. 2010) at the Maidanak Astronomical Observatory (MAO; Uzbekistan).

All MODS observations were taken under good seeing conditions ($0\rlap{.}''5$–$1\rlap{.}''0$). Due to the binocular capabilities of the LBT, the observations in g' and r' were obtained simultaneously with *both* MODS instruments. During the summer of 2021, with the aim of expanding our host galaxy photometry data set, we obtained further U, r', i', z', and R_C imaging with the LBC under variable seeing conditions ($0\rlap{.}''9$–$1\rlap{.}''5$), followed by further MAO observations in the R_C band. The LBT/MODS and LBC imaging data were reduced using the data reduction pipeline developed at INAF–Osservatorio Astronomico di Roma (Fontana et al. 2014), which includes bias subtraction and flat-fielding, bad-pixel and cosmic-ray masking, astrometric calibration, and coaddition. We also downloaded the Gemini/GMOS data at 28 and 46 days reported in Ahumada et al. (2021),[33] and afterward reduced them using the dedicated Gemini pipeline DRAGONS (Labrie et al. 2019). Finally, we downloaded the r'-band Gran Telescopio Canarias (GTC) data at 3.99 days reported in Zhang et al. (2021).[34] The TNG/DOLoRes, GTC, and MAO images were reduced in a standard manner using PyRAF/IRAF tasks (Tody 1993).

The first H-band observations were obtained using the LBT Utility Camera in the Infrared (LUCI; Seifert et al. 2003) imager and spectrograph in conjunction with the Single Conjugate Adaptive Optics Upgrade for LBT (SOUL; Pinna et al. 2021), the second-generation adaptive optics (AO) system at the LBT. Data were obtained 37.1 days after the GRB, close to the expected maximum light of the possible associated SN. Compared to the J and K bands, the H band was preferred for three reasons: (1) there is lower sky and thermal background with respect to the K band; (2) the AO performance is better than that in J, allowing the system to achieve an FWHM $< 0\rlap{.}''1$; and (3) there are no strong emission lines from nonstellar sources or from star formation regions (like Hα in the J band at the redshift of our target), and the host continuum is dominated by light from old, late-type stars. A relatively bright foreground star ($R = 15.06$ mag) $11\rlap{.}''4$ away

---

[33] PI: L. Singer, program GN-2020B-DD-104.
[34] PI: A. J. Castro-Tirado, program GTCMULTIPLE4B-20A.

Table 1
Photometry of the Transient and Host Galaxy

Δt^{a} (days)	Magnitude AB^{b}	Filter	Telescope	Reference^{c}
0.2112	20.86 ± 0.04	g'	ZTF	[1]
0.2304	20.70 ± 0.05	r'	ZTF	"
0.2779	20.96 ± 0.16	g'	ZTF	"
0.7663	>20.2	R_C	Kitab	[2]
1.1458	22.75 ± 0.26	g'	ZTF	[1]
1.2125	>21.3	r'	ZTF	"
1.2875	>21.2	g'	ZTF	"
1.7351	>20.4	R_C	Kitab	[2]
2.183^{d}	23.39 ± 0.16	r'	LBT/MODS	[3]
2.183^{d}	24.08 ± 0.19	g'	LBT/MODS	"
2.27	>23.3	r'	FTN+LCO	[1]
2.28	>23.4	g'	FTN+LCO	"
3.23	24.46 ± 0.12	r'	Lowell	"
3.99	24.51 ± 0.14	r'	GTC	[3, 4]
7.21	>23.5	r'	LBT/MODS	[3]
7.21	>23.6	g'	LBT/MODS	"
15.7	>24.3	R_C	MAO	"
28.3	24.53 ± 0.21	i'	Gemini	[1, 3]
28.3	>25.6	r'	Gemini	[1, 3]
31.9	>25.3	r'	TNG	[3]
33.3	>25.7	r'	LBT/MODS	"
33.3	>25.8	g'	LBT/MODS	"
37.1	24.06 ± 0.20	H	LBT/LUCI	"
46.1	25.36 ± 0.26	i'	Gemini	[1, 3]
46.1	>25.5	r'	Gemini	[1, 3]
50.88	>25.6	r'	LBT/MODS	[3]
50.88	>26.2	g'	LBT/MODS	"
97.0	>24.7	H	LBT/LUCI	"
74.8	22.85 ± 0.11	r'	TNG	"
78.9	22.83 ± 0.04	r'	LBT/MODS	"
78.9	23.12 ± 0.04	g'	LBT/MODS	"
158.5	22.84 ± 0.20	H	LBT/LUCI	"
287	23.36 ± 0.10	U^{e}	LBT/LBC	"
287	22.92 ± 0.08	r'	LBT/LBC	"
287	22.84 ± 0.07	R_C	LBT/LBC	"
287	22.58 ± 0.05	i'	LBT/LBC	"
287	22.25 ± 0.11	z'	LBT/LBC	"
340	22.85 ± 0.07	R_C	MAO	"
382	23.29 ± 0.08	B	MAO	"
391	22.65 ± 0.14	J	LBT/LUCI	"

Notes.
^{a} Midtime after the Fermi/GBM trigger in the observer frame.
^{b} The photometry is not corrected for Galactic extinction. The first part (above the line) is the result of image subtraction and represents the pure transient. The second part below the line has been used to study the host and as reference images for the subtraction.
^{c} [1] Ahumada et al. (2021); [2] GCN 28306 (Belkin et al. 2020a); [3] this work; [4] Zhang et al. (2021).
^{d} These are LBT/MODS acquisition images obtained using a $\sim2' \times 2'$ field of view (FOV) instead of the full $\sim6' \times 6'$. MODS1 was equipped with the g' filter and MODS2 with the r' filter.
^{e} We used $U_{\rm spec}$ for its better sensitivity compared to the $U_{\rm Bessel}$ filter.

from the GRB location (and within the FOV) was used as the AO reference star for the AO system. The AO system achieved an average FWHM of the point-spread function (PSF) $\sim0\rlap{.}''13$. Subsequent observations were able to achieve an FWHM $\sim0\rlap{.}''08$–$0\rlap{.}''13$ (see Section 2.3 for more details). The observations were repeated on 2020 December 1 and 2021 February 7, 97 and 158 days, respectively, after the GRB event.
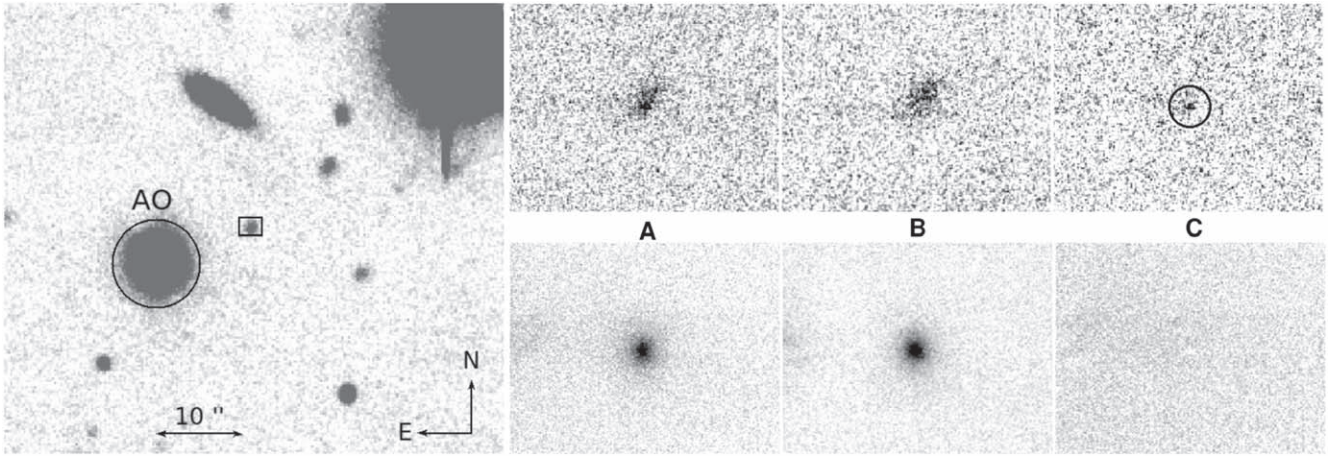
Figure 1. Left: $1' \times 1'$ FOV finding chart derived from the TNG r'-band imaging obtained on 2020 September 27 UT. The star used for AO observations with SOUL and LBT/LUCI is highlighted. The rectangular region is centered on the location of the afterglow, and its angular size is the same as those of the panels on the right. Right: Results of the H-band follow-up using the second-generation SOUL AO system with LUCI-1 at the LBT. The top row shows the location of the host and the GRB (see the region in the left panel). For comparison, the bottom row shows the location of a star in the field. From left to right: (A) the LUCI-1 AO H-band imaging obtained on UT 2020 October 2 (i.e., close to the peak of the SN); (B) the LUCI-1 AO H-band image obtained four months later when only the host is visible; and (C) the subtraction between these two epochs, where the transient is highlighted with a circle (top) and the field star is cleanly subtracted (bottom). The FOV of each panel is $2\rlap{.}''6 \times 2\rlap{.}''0$. The LUCI-1 AO FOV is $30'' \times 30''$. In each panel north is up, and east is to the left. The transient lies at a projected distance of 0.75 kpc from the center of its host galaxy as discussed in Section 3.5.

In 2021 September we also obtained J-band imaging of the host with LBT/LUCI. All near-IR (NIR) data were reduced using the same data reduction pipeline for the LBT/MODS data (Section 2.2), which in the case of LUCI includes dark subtraction, flat-fielding, bad-pixel and cosmic-ray masking, and sky subtraction. Finally, the images were aligned to match the position of the AO reference star and coadded using IRAF tasks. The astrometry was calibrated against field stars in the GAIA DR2 catalog (Gaia Collaboration et al. 2018) and has an astrometric precision of $0\rlap{.}''15$.

All data were analyzed by performing aperture photometry using DAOPHOT and APPHOT under PyRAF/IRAF. For the optical data, the photometric calibration was performed using a set of field stars observed during the fifth MODS epoch (which had photometric conditions) and calibrated against the Sloan Digital Sky Survey DR12 catalog magnitudes of brighter nearby stars (Alam et al. 2015). The NIR photometry was calibrated against the AO reference star and a pair of Two Micron All Sky Survey (Skrutskie et al. 2006) stars observed immediately after the GRB field during the first epoch. The photometric calibration has a standard deviation of 0.02 mag. To err on the side of caution, twice this value was used as the photometric uncertainty.

2.3. Image Subtraction and Photometry of the Transient

To remove the contribution of the host to the afterglow/SN photometry, a reference frame free of any transient light is required. To better investigate any possible contamination from SN light in these earlier observations, the GRB 200826A data sets were compared with those of GRB 980425/SN 1998bw (Galama et al. 1998), which is the standard template for SNe associated with GRBs (GRB-SNe in the following). Following Zeh et al. (2004) and Klose et al. (2019), the observed SN 1998bw light curves were first corrected for Galactic extinction, moved to the rest frame, interpolated with a polynomial curve at steps of 0.5 days, and finally shifted to the GRB

200826A observed bands, r', i', and H, accounting for filter band differences and cosmological k-corrections.

At the time of the last MODS r' observation (78.9 days after the trigger) any SN 1998bw–like GRB-SNe would have had $r' \sim 27$ mag, more than 2 mag fainter than its peak magnitude ($r' \sim 24.7$ mag) at 20–40 days, when the first observations had been obtained. Therefore, it is acceptable to consider the late r' MODS images to be free from any contamination by SN light and they can be used as templates for image subtraction. They can also be used to measure the flux of the host galaxy ($\sim$4 mag brighter in the r' band) instead of the later LBC images, which have a lower signal-to-noise ratio. These LBC images were instead used as reference for the image subtraction of the r' imaging at $\sim$50 days. Similarly, in the H band[35] any SN 1998bw–like GRB-SN contribution at 160 days ($H \sim 26$ mag at the time of our last LBT/LUCI observation) would have been $\sim$2 mag fainter than its peak magnitude ($H \sim 24.3$ mag). Differences of $\sim$2 mag translate to a contribution from the SN to the late-time image of $\sim$0.2 mag. This contribution does not impact the analysis after the image subtraction, but is included in the photometric errors. On the contrary, any SN 1998bw–like GRB-SN would fade by less than 1 mag between 97 and 160 days; thus the last H-band observation (97 days) may also be affected by oversubtraction, and hence may result in a photometric value for the transient that is too faint at 97 days, though the SN is likely too faint to contribute substantially at this point. For completeness we report the resulting upper limit.

For the i' band we note that at the time of the final Gemini observation (at 75 days; see Ahumada et al. 2020b) any SN 1998bw–like GRB-SN would have had $i' \sim 25.5$ mag, just $\sim$1.5–2 mag fainter than the peak magnitude at $\sim$30 days ($\sim$24 mag), which could be acceptable. Instead, this difference is certainly smaller in the case of the Gemini observation at

---

[35] To derive the H-band flux of SN 1998bw at the redshift of GRB 200826A we had to extrapolate the rest-frame I_C-band data of SN 1998bw (e.g., Zeh et al. 2004; Klose et al. 2019).

46 days (see Table 1 and Figure 7). Therefore, we caution that using the value at 75 days as pure host can produce an oversubtraction, in particular at 46 days. Therefore, in the image subtraction of the i' band we used the LBC imaging obtained at 287 days.

Before applying image subtraction, the input and reference images were aligned using the WCSREMAP package.[36] Image subtraction was then performed using a routine based on HOTPANTS[37] (Becker 2015). This algorithm matches the PSF and count flux of both input images. The PSF is modeled via Gaussian functions in subregions of the original image. The software outputs a noise map of the resulting difference image, which is used to derive the uncertainties in the measured fluxes. The routine creates a grid of input Gaussian widths and subregion sizes and searches for the solution with the lowest noise.

In the case of the H-band imaging, the average FWHM during the first epoch was $0\rlap{.}''13$ as measured from the AO reference star in the LUCI-1 FOV[38] and was constant for nearly the entire observation. The small amount of data with larger FWHMs was not used for analysis. A total of 1180 s of exposure time with FWHM $\sim 0\rlap{.}''13$ was used for analysis. For the other epochs the FWHMs ranged from $0\rlap{.}''08$ to $0\rlap{.}''15$. Therefore, only exposures with an FWHM of the AO reference star $<0\rlap{.}''13$ (to match the first epoch) were selected. This yielded a combined image with a total integration time of 2400 s and 2700 s for the second and last epochs, respectively. In particular, the AO reference star in the last epoch had an FWHM $\sim 0\rlap{.}''10$, and this was used as the template for image subtraction. In contrast to the optical images, only two stars (the AO reference star and another star close to it) were useful for mapping the PSF and flux. Unfortunately, this impacts the optimal use of HOTPANTS for scaling the template image to the flux of the science image. Instead, a better result was obtained using the PSF-MATCH task under IRAF and by scaling the images to have the same flux for the two stars. The image subtraction of the two H-band images shows a transient located at R.A. (J2000) = $00^h27^m08\rlap{.}^s55$, decl. (J2000) = $+34°$ $01'38\rlap{.}''2$ with an uncertainty of $0\rlap{.}''15$ and calibrated against the MODS images (Figure 1). This is consistent with the position reported by Ahumada et al. (2020a).

All image-subtracted data have been analyzed using aperture photometry as detailed in Section 2.2. Table 1 provides a summary of all the photometry of the transient and the host galaxy including values collected from the literature.

Apparent magnitudes were corrected for Galactic extinction using the Cardelli et al. (1989) interstellar extinction curve, a total-to-selective extinction of $R_V = 3.1$, and a reddening along the line of sight of $E(B-V) = 0.058$ mag (Schlafly & Finkbeiner 2011).

2.4. Modeling of the Light Curve and SED

Although the g' and r' light curves are quite sparse, they can be modeled with a single power law with $\alpha = 0.94 \pm 0.05$. However, this model implies that the late afterglow is brighter than the deep r' upper limits obtained at ~ 30 days after subtraction of the host galaxy contribution. Therefore, the data were modeled with a smoothly broken power law (Beuermann et al. 1999) (Figure 2). The last detections in the g' and r' bands
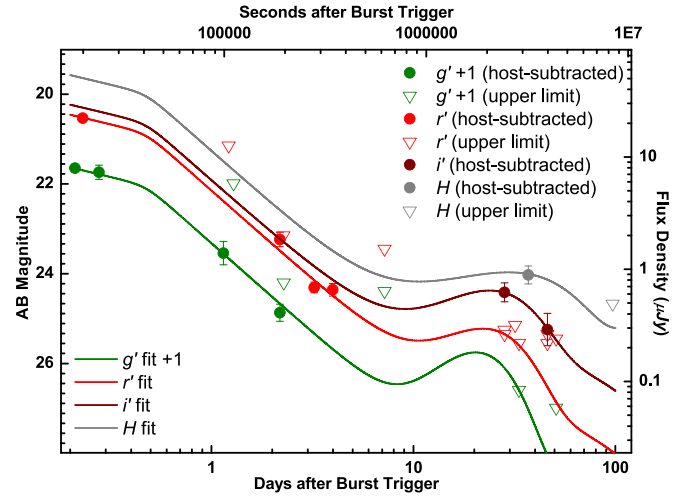
Figure 2. Light curves of the afterglow and SN component of GRB 200826A in the g', r', i', and H bands, after subtraction of the host galaxy contribution. The data have been modeled with a smoothly broken power law for the afterglow, and with an SN 1998bw template redshifted to $z = 0.7486$ for the SN phase. In the g' and r' bands, we forced the individual SN light-curve components to go through the most significant deep upper limit in each band to obtain upper limits on the potential SN luminosity. Note the g' band is offset by 1 mag for reasons of clarity. See Table 1 and Sections 2.4 and 3.3 for more information.

are at ≈ 2.2 and ≈ 4 days (observer-frame). Using SN 1998bw as an SN template (see below for more details), the SN itself would have had $g' = 29.8$ mag and $r' = 26.9$ mag at 2.2 days and 4 days, respectively. Therefore, it can safely be assumed to not contribute significantly to the optical transient and can be ignored in the afterglow fitting. This yielded decay slopes $\alpha_1 = 0.43 \pm 0.55$ and $\alpha_2 = 1.59 \pm 0.20$, with a break time $t_b = 0.47 \pm 0.24$ days, and the break smoothness $n = 10$ fixed. The post-break decay slope easily accommodates the magnitude upper limits at later times, with values beyond $r' \sim 27.8$ mag and $g' \sim 28.3$ mag at ~ 30 days. Therefore, any late emission detected via subtraction is not from the afterglow.

To investigate whether the optical data are affected by local dust extinction along the line of sight, the SED was modeled spanning the optical to the X-ray band. All Swift/XRT data available were used, which have a mean arrival time of 65,840 s (0.762 days), along with the g' and r' bands obtained from the broken power-law fit (see above), and thus are free from host contamination. The redshift was fixed to match that of the host galaxy and the Galactic hydrogen column density was set to $N_H = 6.02 \times 10^{20}$ cm^{-2} (Willingale et al. 2013). The optical-to-X-ray SED is well fit ($\chi^2/\mathrm{dof} = 33/47$) by a power law with a spectral index $\beta = 0.79 \pm 0.03$ without the need for additional dust extinction and gas absorption to improve the fit. The negligible dust extinction is well supported by the optical-to-X-ray spectral index $\beta_{OX} > 0.5$ (Jakobsson et al. 2004; Rossi et al. 2012). The optical-to-X-ray spectral slope was then used to extrapolate the late-time brightness in the i' and H bands. For the first i' detection at 28 days, the brightness of the projected afterglow was 27.6 mag, 3.2 mag fainter than the detection. The H-band afterglow is $H \sim 27.4$ mag at 37 days, 3.4 mag fainter than the detection.

To consider also the contribution of an emerging SN component, we followed the work of Zeh et al. (2004) and Klose et al. (2019), and modeled the afterglow and SN component in a joint g', r', i', and H fit (rest-frame far-UV, U,

B, and z' bands). The analytical light curve of SN 1998bw and the k, s parameterization was used (see Section 2.4). The parameter k is the luminosity factor and it describes the observed luminosity ratio between the GRB-SN at peak time and the SN template in the considered band. The parameter s is a stretch factor with respect to the used template.[39] The observer-frame g' band (rest-frame far-UV) is not covered by observations in the case of SN 1998bw (in contrast to the observer-frame r' band, which is the rest-frame U band), so we assume that the flux density of the SN falls as ν^{-3} to extrapolate and derive the corresponding far-UV SN 1998bw template (e.g., Klose et al. 2019). Note that the g' and r' data points in Figure 2 after 2.2 and 4 days (observer-frame) are upper limits only. In order to constrain the flux density of a possible SN contribution in these bands, we considered these limits as proxy detections in the modeling. We also remind the reader that the i'- and H-band afterglow light curves have been spectrally extrapolated (see above) because there are no observations in these bands during the afterglow phase. The sparse data in i' and H preclude determining the precise temporal evolution of the late emission, but do not preclude determining more information on the luminosity. The stretch factor was fixed at $s = 1$ for all bands and the luminosity factor k was allowed to vary freely and individually in each band. The results of this joint fit are presented and discussed in Section 3.3.

3. Results

A summary of the photometry of the transient resulting from the host subtraction analyses is presented in Table 1. NIR emission (rest-frame ~ 0.93 μm) is clearly detected 37 days (21.22 days rest frame) after the burst (see also Figure 1). Thanks to our late reference images obtained with the LBC, which are free from SN light, we also detect a bump in the i' band at 28.3 and 46.1 days (14.9 and 26.3 days rest frame). Ahumada et al. (2021) reported a bump that is ~ 1 mag fainter and they did not find the transient in the second epoch. This last detection allows us to better constrain the late evolution of the transient. In the r' band, the presence of a bump could only be constrained beyond the 3σ mag limits of $r' > 25.5$ mag, $r' > 25.3$ mag, and $r' > 25.7$ mag in the first Gemini, TNG, and LBT epochs, respectively (the results presented here supersede the preliminary results of Rossi et al. 2020a).

3.1. GRB 200826A

The duration of GRB 200826A, as reported by the different detectors and in different energy bands, is 1–2 s (see Section 1), placing it right at the divide between SGRBs and LGRBs in the duration distribution commonly used to distinguish between these two classes (but see de Ugarte Postigo et al. 2011; Bromberg et al. 2012).

There are other events that lie between the two populations, but none has an observed T_{90} shorter than 2 s and an associated SN that clearly points to a collapsar origin. For example, GRB 090426 ($z = 2.609$) has a duration shorter than 2 s but also has characteristics typical of LGRBs including softer spectra, a bright afterglow, and a blue and low-mass host (Antonelli et al. 2009; Nicuesa Guelbenzu et al. 2011, 2012; Thöne et al. 2011;

D. A. Kann et al. 2022, in preparation). It could be argued that one should consider the intrinsic duration in the rest frame ($T_{90,i}$). Doing so, the duration of GRB 200826A would be between 0.39 (Konus-Wind) and 0.57 (GBM) s, i.e., well below 2 s. The only other GRB with an associated SN that could be classified as short because of its intrinsic duration ($T_{90,i} = 2.4$ s, $z = 0.86$) is GRB 040924 (Huang et al. 2005; Soderberg et al. 2006; Wiersema et al. 2008). Many other cases exist at high redshift like GRB 080913 (Greiner et al. 2009; Zhang et al. 2009), but the redshift is too high to search for the associated SN (at least with the current facilities).

Bromberg et al. (2012) showed that the 2 s duration commonly used to separate collapsars and noncollapsars is inconsistent with the duration distributions of Swift and Fermi GRBs and only holds for old CGRO/BATSE GRBs. However, analysis of the Konus-Wind data (Svinkin et al. 2020) showed that GRB 200826A has a duration typical of SGRBs. Thus, the short duration of GRB 200826A is instrument-independent. In this case T_{90} alone is insufficient to determine which population GRB 200826A is best associated with. Another feature typical of LGRBs is a nonnegligible spectral lag (Norris et al. 1996). This parameter has been calculated and the details are provided in the Appendix. We obtain a spectral lag of 96 ± 38 ms, which lies between the values found by Ahumada et al. (2021) and Zhang et al. (2021). In agreement with their analysis, we conclude that the measured spectral lag is more typical of LGRBs.

It is only when both the spectral properties of GRB 200826A and its location in the hardness–duration plane are considered does it appear to be more similar to "long" GRBs. However, if this is indeed the shortest "long" GRB associated with an SN, then additional evidence is needed to demonstrate that it does not belong to the SGRB class. Such a result would challenge the standard paradigm for SGRB and LGRB progenitors.

In this respect, a very useful tool is the location of a GRB in the $E_{p,i}$–E_{iso} plane,[40] where LGRBs follow a strong correlation known as the "Amati relation" (Amati et al. 2002; Amati 2006). In comparison, SGRBs populate a different region in this plane (e.g., D'Avanzo et al. 2014; Minaev & Pozanenko 2020a). Therefore, the fluence and spectral parameters reported by the Konus-Wind and Fermi/GBM teams were used (Mangan et al. 2020; Ridnaia et al. 2020; Svinkin et al. 2020) to compute the values of $E_{p,i}$ and E_{iso}, and their uncertainties, for GRB 200826A. As can be seen in Figure 3, this event is fully consistent with the $E_{p,i}$–E_{iso} relation followed by LGRBs. This further supports the hypothesis that it is actually a "long" GRB with a duration in the short tail of the distribution.

Recently, the energy–hardness (EH) parameter—a combination of $E_{p,i}$ and E_{iso} (EH $= E_{p,i}E_{iso}^{-0.4}$)—was introduced in Minaev & Pozanenko (2020a). Although GRB 200826A is placed inside the 95% cluster region of long bursts in the $T_{90,i}$–EH diagram (Figure 4), it is evident that this does not permit an unambiguous classification of a burst close to the cluster region intersection (see also Zhang et al. 2021 for a similar analysis and conclusion). Also the position in the $E_{p,i}$–E_{iso} plane may not be sufficient for classification. Indeed, interesting examples such as GRB 201221D[41] (Agüí Fernández

---

[39] As in Section 2.3, cosmological effects such as k-correction were considered when the SN template was moved to the redshift of our GRB. For further details on the method see Zeh et al. (2004) and Klose et al. (2019), and references therein.

[40] $E_{p,i} = E_{p,obs}(1 + z)$ is the rest-frame photon energy at which the νF_ν spectrum peaks, and E_{iso} is the isotropic-equivalent radiated energy as measured in a "bolometric" band, usually 1 keV–10 MeV in the rest frame.
[41] With a rest-frame Fermi/GBM $T_{90} = 0.068$ s (Hamburg et al. 2020), and a Swift/BAT $T_{90} = 0.078 \pm 0.0196$ s (Krimm et al. 2020).
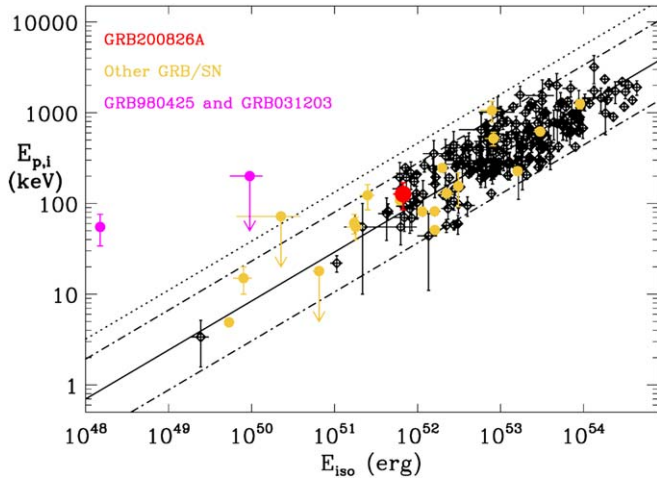
Figure 3. GRB 200826A (red) in the $E_{p,i}$–E_{iso} plane. GRBs with an associated SN are highlighted in amber, outliers in magenta (see Section 3.1). The GRB data is from Amati et al. (2019).
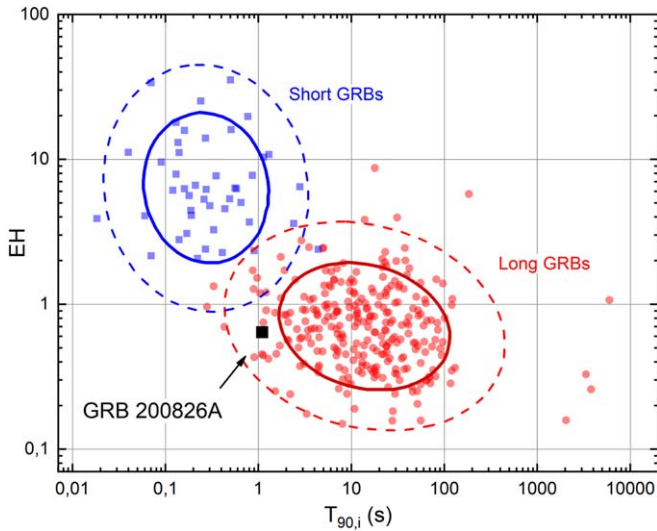

Figure 4. The $T_{90,i}$–EH diagram for SGRBs (blue squares) and LGRBs (red circles) with corresponding cluster analysis results. The 68% and 95% confidence regions are shown by bold solid and thin dashed curves. Data from Minaev & Pozanenko (2020a, 2020b).

et al. 2021) exist which follow the $E_{p,i}$–E_{iso} relation for LGRBs but are in the SGRB region in the $T_{90,i}$–EH diagram.

3.2. The Afterglow of GRB 200826A

A well-known result is that most SGRB afterglows are much fainter than LGRB afterglows (Gehrels et al. 2008; Nysewander et al. 2009; Kann et al. 2010, 2011). Following the method of Kann et al. (2006), using a spectral slope of $\beta = 0.79$ and no line-of-sight extinction, in Figure 5 the optical afterglow of GRB 200826A is compared with a large sample of SGRB and LGRB optical afterglows (taken from Kann et al. 2006, 2010, 2011; Agüí Fernández et al. 2021; D. A. Kann et al. 2022, in preparation). Similarly, in Figure 6 the X-ray emission of GRB 200826A is compared with that of ∼500 GRB afterglows (of which 38 are of SGRBs) detected in at least two epochs and with known redshift. The X-ray light curves were obtained from the Swift Burst Analyser[42] (Evans et al. 2010)

---

[42] https://www.swift.ac.uk/burst_analyser/
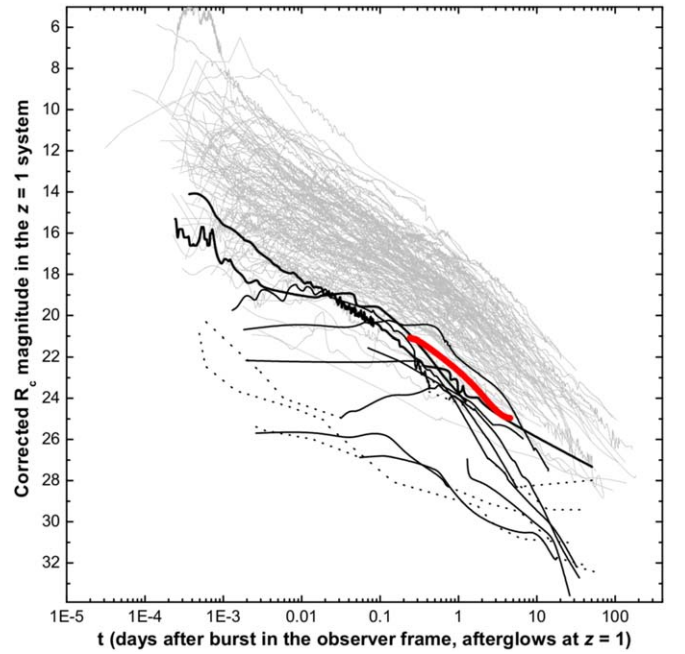
Figure 5. The optical afterglow of GRB 200826A (red line) compared with the sample of extinction-corrected afterglows shifted to $z = 1$ from Kann et al. (2010, 2011) and D. A. Kann 2022, in preparation. Here, time and magnitudes are given in the observer frame, but assuming all GRBs are at $z = 1$ in a perfectly transparent universe. The light gray lines are LGRBs, and the thicker black lines are SGRBs with secure redshifts (solid lines connect detections, and dashed lines connect upper limits). All magnitudes are Vega magnitudes. The afterglow of GRB 200826A lies intermediately between those of secure LGRBs and secure SGRBs.
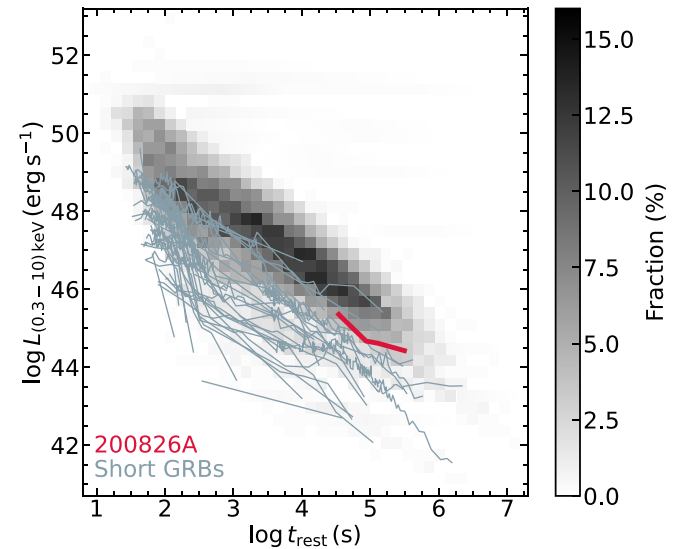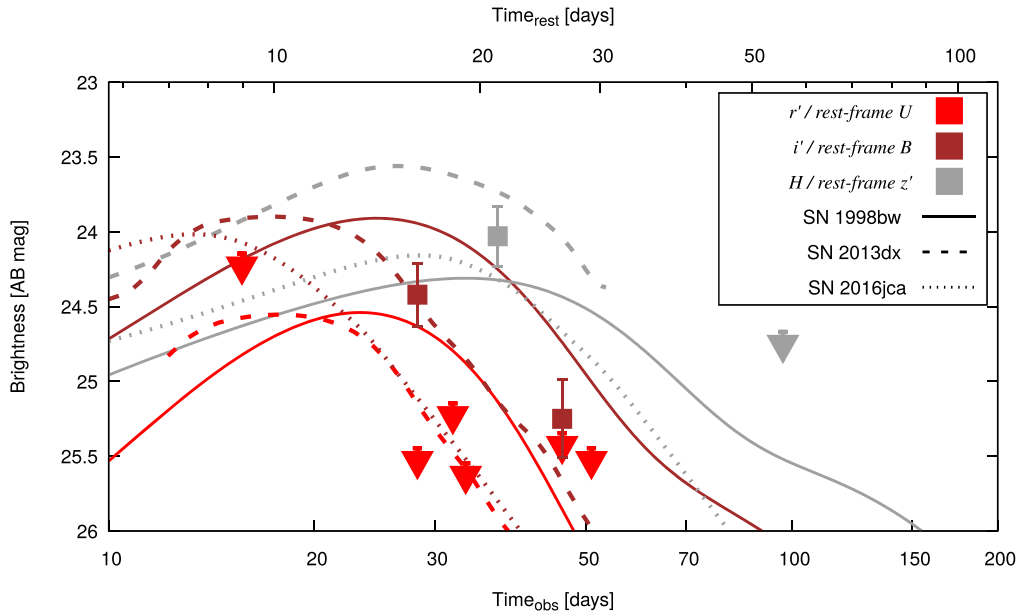

Figure 6. The X-ray afterglow of GRB 200826A (red line) in the context of the X-ray afterglows of 449 Swift GRBs with known redshifts. This event could be followed up by Swift/XRT only after 10 ks, but the few data points obtained show that the luminosity of GRB 200826A is between the long and short populations. The gray scale on the right is used to convert a given luminosity and time into a fraction of bursts.

and put in the same frame using the method described in Schulze et al. (2014). The afterglow of GRB 200826A is among the faintest afterglows of LGRBs but also among the brightest ones of SGRBs, in both the X-ray and optical bands. Thus, using the afterglow luminosity is not a good method for classifying, or understanding the nature of, this burst.

Figure 7. Light curve in i' and H bands after removing the host component via image subtraction (see Table 1). Only data after 10 days (observer-frame) are shown. The data are corrected for Galactic extinction (see Section 2.3). The SN light-curve templates obtained from SN 1998bw, SN 2013dx, and SN 2016jca are shown for comparison and to stress the large range of variability and color of GRB-SNe (see Section 3.3). Downward-pointing triangles are upper limits.

3.3. The Late Bump as SN Emission

Although the sparse data precludes determining the evolution of the late bump seen in the transient light curve, a comparison can be made with other GRB-SNe to look for similarities. This comparison includes GRB 980425/SN 1998bw (Galama et al. 1998), GRB 060218/SN 2006aj (Ferrero et al. 2006), GRB 100316D/SN 2010bh (Olivares et al. 2012), GRB 130702A/SN 2013dx (D'Elia et al. 2015; Toy et al. 2016; Volnova et al. 2017; Mazzali et al. 2021), and GRB 161219B/SN 2016jca (Cano et al. 2017b; Ashall et al. 2019). In Figure 7 we show only those GRB-SNe with comparable peak luminosities and colors, including SN 1998bw, which has been used to also fit extreme events such as SN 2011kl (Greiner et al. 2015; Kann et al. 2019) and the SN bump of GRB 140506A (Kann et al. 2021). Due to the nonnegligible redshift of GRB 200826A, the observed r'-, i'-, and H-band data sets correspond approximately to the rest-frame U, B, and z' bands, respectively. In the following comparison, we will refer to these rest-frame bands.

The SN associated with GRB 200826A appears fainter than SN 1998bw in the rest-frame B band, but is of comparable luminosity to or slightly brighter ($\lesssim$0.5 mag) than SN 1998bw in the rest-frame z band. The most striking feature is the suppression in the rest-frame U band, by at least 1 mag compared to SN 1998bw at 28 days. This prompted a further investigation into GRB-SNe with redder colors, and produced possible agreement with GRB 130702A/SN 2013dx. This GRB-SN (like GRB 161219B/SN 2016jca and possibly GRB 050525A/SN 2005nc; Della Valle et al. 2006) is characterized by a rise-to-maximum time $\Delta t \lesssim 15$ days in the respective rest frame (e.g., Belkin et al. 2020b), which is a parameter related to properties of progenitor stars (e.g., González-Gaitán et al. 2015).

In Section 2.4 we have modeled the late light curve considering the analytical light curve of SN 1998bw and the k, s parameterization following the work of Zeh et al. (2004) and Klose et al. (2019), which allows us to place quantitative

constraints on the above analysis. We remind the reader that there are no detections in g' and r' after 2.2 and 4 days (observer-frame), and thus with our modeling we can only place deep upper limits on the flux density of the SN contribution in these bands (see Figure 2). In terms of luminosity, a potential SN contribution in the rest-frame far-UV (observed g' band) is found as $k_{g'} < 1.5$, an unremarkable limit to its luminosity. Therefore, although the spectral slope of the extrapolation mentioned above is insecure, this does not have any significant impact on our modeling. However, there is clear UV suppression in the rest-frame U band: we find $k_{r'} < 0.43$, implying that the SN associated with GRB 200826A is less than half as luminous as SN 1998bw in the same rest-frame band. In the rest-frame B band the suppression is also strong compared to SN 1998bw with $k_{i'} = 0.56 \pm 0.10$. The rest-frame z'-band detection (observed H-band) is, however, marginally brighter than SN 1998bw ($k_H = 1.18 \pm 0.22$). Moreover, it lies close to the SN peak for $s = 1$, and thus a significantly faster or slower SN would be even brighter. When compared with the list of k, s values of Klose et al. (2019) and Cano et al. (2017a) the k factor ranges between 0.5 and 2. This provides plausible support for an SN.

3.4. Possible KN Emission

In Figure 8, the late-time photometry of the transient is compared with the light curve of AT 2017gfo, the KN associated with the binary NS merger GW170817 and the SGRB 170817A (Abbott et al. 2017c). The KN light curves are obtained from observed spectra shifted and scaled to the same redshift of GRB 200826A, following the method described in Rossi et al. (2020b). The comparison shows that the luminosity of the transient was at all times at least 3 mag brighter than the peak luminosity of AT 2017gfo. This is not extraordinary, because KNe $\gtrsim$10 times more luminous in the optical have been claimed to exist (e.g., Gao et al. 2017; Fong et al. 2021). However, what makes this event very different from all KNe observed so far is its slower temporal evolution: assuming that
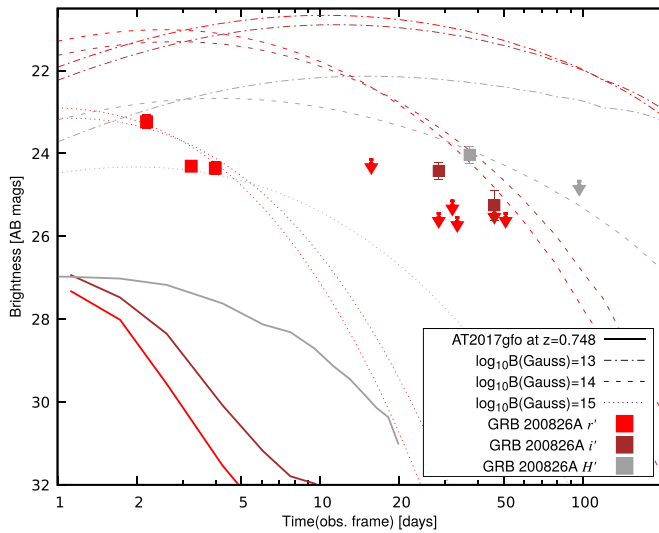
Figure 8. Light curves of the optical transient that followed GRB 200826A after host subtraction compared with the light curves of AT 2017gfo (solid lines) from Rossi et al. (2020b) and with theoretical KN light curves boosted by a magnetar from Perego et al. (2017) with three different magnetic field strengths (dotted, dashed, and dotted–dashed lines; Section 3.4). Downward-pointing triangles are upper limits.

the rest-frame B-band detection (i'-band detection in the observer frame) is close to maximum light, i.e., ~ 16 days in the rest frame, the peak would be more than ~ 15 days later than that of AT 2017gfo. The analysis below investigates whether such behavior is theoretically possible.

Modeling of KNe powered by radioactive decay of r-process nuclei shows that KNe produced by nearly equal-mass binary NS mergers are expected to have peak times and magnitudes similar (within a few days and one or two magnitudes, respectively) to the ones observed in AT 2017gfo, especially in the case of face-on mergers characterized by lanthanide-free high-latitude ejecta (e.g., Radice et al. 2018b; Kawaguchi et al. 2020). Viewing angle and composition effects possibly decrease the KN luminosity as compared with face-on configurations (Korobkin et al. 2021). In the case of very unequal-mass binary NS or black hole–NS mergers, the peak evolution can be slower, especially in the rest-frame NIR bands, but with similar peak magnitudes (e.g., Barbieri et al. 2019; Bernuzzi et al. 2020; Kawaguchi et al. 2020; Zhu et al. 2020). These theoretical results seem to also disfavor the interpretation of the observed transient as a KN powered by radioactive decay.

However, it is known from several studies (e.g., Gompertz et al. 2018; Ascenzi et al. 2019; Rossi et al. 2020b; Rastinejad et al. 2021) that the distribution of luminosities covers a large range, and some KNe can be 10 times more luminous than AT 2017gfo, such as those associated with GRBs 060614 and 050724 (Gao et al. 2017). Even more extreme cases that are ~ 100 times more luminous have been claimed to exist in association with GRB 070714B (Gao et al. 2017) and more recently with GRB 200522A (Fong et al. 2021; O'Connor et al. 2021), although the evidence is not very strong. To achieve this high blue luminosity, the KN can be boosted by energy deposition from a magnetar remnant. Indeed, long-lived merger remnants could have a significant impact on KN light curves. While larger amounts of ejecta, expelled due to angular momentum excess, can increase peak magnitudes, times, and widths only marginally (e.g., Radice et al. 2018a), the presence

of a fast-rotating magnetar (in addition to its being a possible GRB central engine) can boost the KN luminosity via spin-down luminosity (Yu et al. 2013; Metzger & Piro 2014; Siegel & Ciolfi 2016).

To explore this scenario, the KN model presented in Perego et al. (2017) was used and extended to consider spin-down energy injection, as well as sources at cosmological distances for which the fluxes, the (thermal) spectra, and the observer time were corrected for the cosmological redshift. The computed KN light curves are shown in Figure 8. For simplicity, a spherically symmetric ejecta model was considered for which $0.02\,M_\odot$ of matter expands homologously at $0.2c$. Given that the adopted model foresees the presence of a long-lived magnetar, an effective gray opacity $\kappa = 1\ \mathrm{cm}^2\ \mathrm{g}^{-1}$, typical of lanthanide-poor ejecta, was assumed. $P_0 = 0.7$ ms was fixed as a typical initial rotation period (Radice et al. 2018a), while the strength of the magnetic field B and the energy deposition efficiency for the spin-down luminosity ϵ_{th} were varied to obtain plausible agreement with the observations. A reasonable match for $B \sim 10^{14}$ G and $\epsilon_{\mathrm{th}} = 0.03$ is shown in Figure 8. For the considered bands, larger magnetic field strengths ($B = 10^{15}$ G) result in lower, more rapidly declining peaks, and a plausible match with the data would require $\epsilon_{\mathrm{th}} \gtrsim 1$. Weaker field strengths ($B = 10^{13}$ G), on the other hand, produce more luminous, more slowly evolving peaks, which plausibly match the data for $\epsilon \lesssim 0.001$. The ejecta properties also influence the light curves, but less significantly.

The calculations suggest that the observed transient could be compatible with the late emission of a spin-down-powered KN for plausible values of the magnetic field and thermalization efficiency. Unfortunately, all of the magnetically boosted KN models fail to explain the red color of the transient, and in particular the strong UV suppression observed in the observer-frame r' band, although modeling greatly simplifies the ejecta and the emission properties, particularly the opacity. But most importantly, during the first 10 days the theoretical KN is comparable to or brighter than the observed data without accounting for the afterglow. Therefore, the magnetically boosted KN models are excluded.

3.5. The Host Galaxy

As first reported in Rothberg et al. (2020a, 2020b), the continuum of the host galaxy was clearly detected between $0.38\,\mu$m and $0.98\,\mu$m. A redshift of $z = 0.748577 \pm 0.000065$ was determined from the simultaneous detection of the following emission lines: [O II], [O III], and [Ne III] doublets; He I $\lambda3889$; and Balmer Hδ $\lambda4101$, Hγ $\lambda4340$, and Hβ $\lambda4861$ (Figure 9). The fluxes of the lines were measured using the slinefit code (Schreiber et al. 2018), which also allows correction of the Balmer-line fluxes for the underlying stellar absorption. All the measured fluxes are reported in Table 2. The absorption lines of the Mg II $\lambda\lambda2796$, 2803 doublet were also detected at a lower redshift ($z = 0.7462 \pm 0.0002$), which may possibly imply that they are due to an intervening Mg II absorber along the line of sight (Vergani et al. 2009; Christensen et al. 2017). The rest-frame equivalent width for both lines in the doublet is $W_{\mathrm{rest}} = 2.4 \pm 0.6$ Å.

Using the derived redshift as a fixed input, the optical/NIR SED of the host galaxy was modeled (Table 1) with the code Le PHARE (Arnouts et al. 1999; Ilbert et al. 2006). The best fit
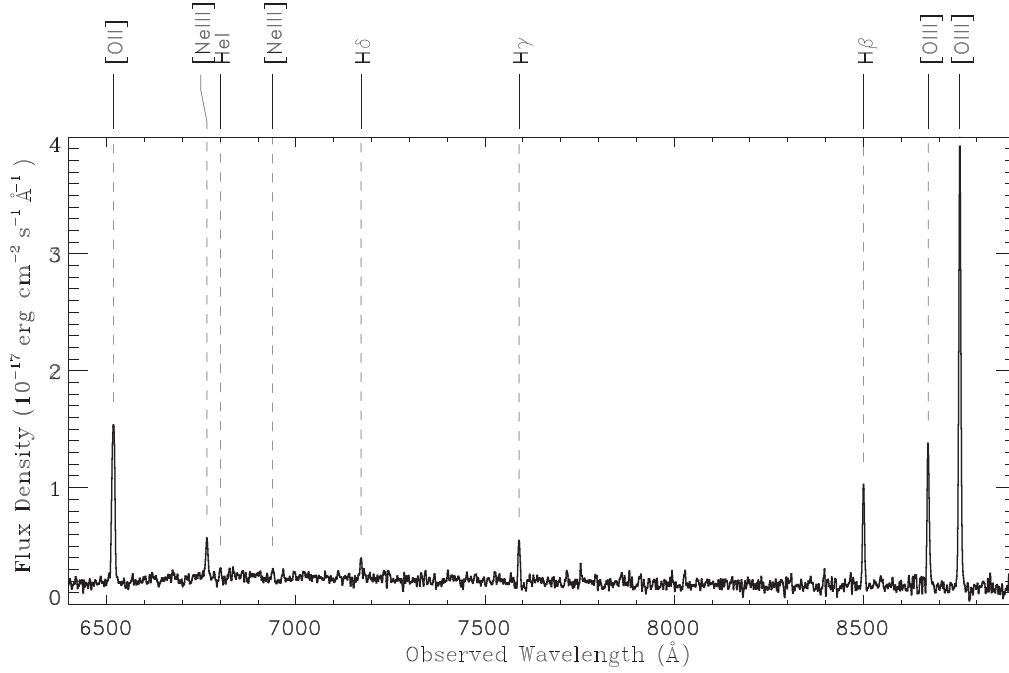
Figure 9. LBT/MODS-observed spectrum of the host galaxy of GRB 200826A binned by 2.5 Å for presentation purposes. The detected emission lines are marked. (The data used to create this figure are available.)
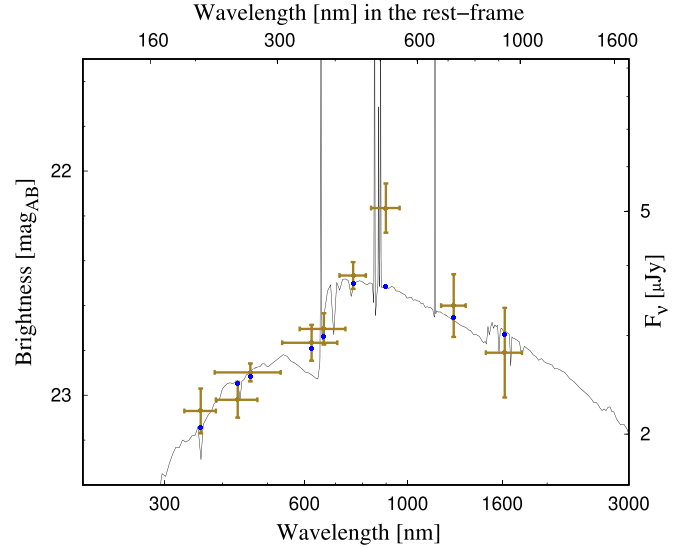
Table 2
Emission Lines and Their Measured Fluxes Corrected for Galactic Extinction

Lines	Flux (10^{-17} erg cm^{-2} s^{-1})
[OII] $\lambda 3727$	12.6 ± 0.4
[Ne III] $\lambda 3869$	2.1 ± 0.4
He I $\lambda 3889$	1.2 ± 0.4
[Ne III] $\lambda 3968$	1.2 ± 0.4
Hδ $\lambda 4102$	1.8 ± 0.4
Hγ $\lambda 4340$	2.8 ± 0.4
Hβ $\lambda 4861$	6.4 ± 0.6
[O II] $\lambda 4959$	8.0 ± 0.3
[O III] $\lambda 5007$	26.5 ± 0.9

Note. The FWHM of the lines is $\sim$6.1 Å. The mean redshift of the emission lines is $z = 0.748577 \pm 0.000065$.

(χ^2/dof = 2.2/9) points to a galaxy dominated by a young population ($0.04^{+0.08}_{-0.02}$ Gyr) with global dust reddening $E(B-V) \sim$ 0.2 mag using the Small Magellanic Cloud (SMC) curves from Pei (1992) and low stellar mass $\log M_*/M_\odot = 8.6 \pm 0.2$ (Figure 10). The B-band dust-corrected absolute magnitude is $M_B = -20.01$ mag and the star formation rate is SFR = $13.0^{+10.9}_{-6.0}$ $M_\odot$ yr^{-1}. With this large uncertainty, this SFR is consistent with what is measured from the emission lines (see below). The dust extinction is in agreement with the broad range of values found for LGRB hosts, also in comparison with the SFR (Hunt et al. 2014; Japelj et al. 2016). It is different from the afterglow-derived negligible extinction, indicating that the GRB sight line might be crossing a relatively dust-free region (e.g., by being placed at the front side of the host galaxy). Compared to Ahumada et al. (2021), we find a mass that is a factor 10 lower. The computed lower mass is most likely due to the fact that the NIR observations were obtained

Figure 10. Le PHARE modeling discussed in Section 3.5 of the SED obtained from the final LBT/LBC $UR_C i'z'$, MAO B, LBT/MODS $g'r'$, LBT/LUCI J, and LBT/LUCI+SOUL H band imaging (see Table 1). The blue points indicate where the photometry would be placed according to the best-fit model and without a contribution from emission lines.

sufficiently late to be free of any contributions from the transient.

Using the Balmer decrement, and assuming the theoretical values for the Hγ/Hβ and Hδ/Hβ ratios, in the absence of dust, for case B recombination at a gas temperature of 10^4 K (Osterbrock 1989), and a Milky Way (MW) extinction law[43] (Pei 1992) with $R_V = 3.1$, we derive an $E(B-V)$ of $\sim$0.16 mag

---

[43] Note that the difference between the MW and SMC or LMC extinction laws is small in the wavelength range of Hδ to Hβ.

and an $A_V \sim 0.5$ mag. Using extinction-corrected Hβ and [O II] fluxes and the prescriptions provided by Kennicutt (1998) and Savaglio et al. (2009), the resulting SFR of the host galaxy is SFR $\sim 4.0\, M_\odot\, yr^{-1}$. The SFR determined from the line fluxes is within 2σ of that derived from SED fitting. The high SFR obtained from the two separate methods implies a specific SFR (sSFR; SFR per unit stellar mass) of $1-3 \times 10^{-8}\, yr^{-1}$, among the highest measured so far in the LGRB host population (e.g., Savaglio et al. 2009; Perley et al. 2013; Hunt et al. 2014; Vergani et al. 2015; Japelj et al. 2016; Schulze et al. 2018; Modjaz et al. 2020). For comparison, this sSFR is about two orders of magnitude higher than that for the Large Magellanic Cloud (LMC). Moreover, if the derived SFR were constant, this would imply that the time required for the host to build the measured stellar mass would be about 0.03–0.1 Gyr, which is consistent with the upper limit obtained from the SED best fit. Using the appropriate diagnostic tools in Lamareille (2010), Trouille et al. (2011), and Marocco et al. (2011) the presence of an active galactic nucleus, which may mimic a high SFR, can be confidently excluded.

The diagnostic ratios of the [O II], [O III], and Hβ emission lines were used to derive the gas metallicity in the host galaxy. Many calibrators have been proposed in the past (for a review, see Maiolino & Mannucci 2019); the method proposed by Curti et al. (2017) was adopted, which computes the best-fit metallicity by minimizing χ^2 in the space defined by the different possible diagnostics given the available emission lines. This yielded $12 + \log(O/H) = 8.31 \pm 0.02$. This is in agreement with the value of $12 + \log(O/H) \simeq 8.3$ obtained from using the [Ne III] $\lambda 3869$/[O II] line ratio (e.g., Bian et al. 2018), a method that has more uncertainties. The resulting subsolar metallicity ($Z/Z_\odot \simeq 0.4$) is consistent with the values derived for LGRB hosts at similar redshift (Japelj et al. 2016). However, we note that the redshift evolution of the mass–metallicity relation in normal star-forming galaxies derived by Bellstedt et al. (2021) shows that galaxies at $z = 0.62$ or 0.8 and stellar masses similar to that of the GRB 200826A host have a typical metallicity of about $12 + \log(O/H) = 7.85$ or 7.80, respectively, significantly below our measured value. Taken together, these results indicate that the host galaxy of GRB 200826A is characterized by a typical metallicity but a higher than usual SFR and sSFR for an LGRB host.

For the adopted cosmological parameters and using the last deep H-band observation, the half-light radius of the host galaxy is $R_h = 0''.16$ or 1.2 kpc at the redshift of the GRB. This size is consistent with LGRB hosts of similar masses (Kelly et al. 2014). The high angular resolution from the LUCI-AO observations also makes it possible to measure the GRB-SN position within the host. The transient has an offset of $R = 0''.1$ from the center of the host, which corresponds to 0.75 kpc. This corresponds to a normalized offset $R/R_h = 0.62$, which is also consistent with the vast majority of LGRBs (e.g., Bloom et al. 2002; Blanchard et al. 2016).

4. Discussion

Additional support for the collapsar scenario was recently reported by Rhodes et al. (2021). By analyzing the radio and X-ray light curves, they found evidence of a sharp rise peaking at 4–5 days after the trigger in the radio bands. Within the LGRB/collapsar scenario, they proposed that the peak is produced by the synchrotron self-absorption frequency moving through the radio band, resulting from the forward shock

propagating into a wind medium. Is our modeling of the afterglow and optical-to-X-ray SED in agreement with their claim? The spectral slope of $\beta = 0.79$ we found in Section 2.4 favors emission in both the optical and X-ray bands that is below the cooling frequency, i.e., $\beta = (p - 1)/2$, with $p = 2.58 \pm 0.06$ following Sari et al. (1998), a typical value for synchrotron emission in GRB afterglows. If the afterglow is in the post-break phase when we measure the SED, the spectral and decay slopes are difficult to justify within the standard afterglow theory. Therefore, assuming that the afterglow is still in the pre-break phase (spherical expansion) the temporal decay index for emission below the cooling break is $\alpha = 3(p - 1)/4$ and $\alpha = (3p - 1)/4$ for an interstellar medium and wind environment, respectively. Using $\alpha = 1.59 \pm 0.20$, we obtain $p = 3.12 \pm 0.27$ and $p = 2.45 \pm 0.27$, respectively (Granot & Sari 2002), and thus we find that propagation into a wind environment could well explain both spectral index and light-curve decay, in support of the analysis of Rhodes et al. (2021). While steep, a pre-break decay of $\alpha = 1.59$ is not unheard of— the sample of Zeh et al. (2006) contains two out of 16 well-defined light curves with $\alpha_1 \approx 1.75$ followed by clear breaks and much steeper post-break decay slopes $\alpha_2 \approx 3$. In such a case, the early shallower decay of the afterglow of GRB 200826A could represent an optical plateau (e.g., Dainotti et al. 2020; S. Ronchini et al. 2022, in preparation). In this scenario the late shallow decay observed in the X-rays can be explained as energy injection from a newborn magnetar (see also Zhang et al. 2021), but also by the receding cooling frequency after the passage of the wind termination-shock radius (e.g., Schulze et al. 2011).

All arguments presented in this work point to a massive-star origin consistent with a collapsar event despite the very short duration. Several theoretical routes have been presented to explain this. In one of the scenarios discussed by Zhang et al. (2021) and by Ahumada et al. (2021) to explain the short duration of the burst, if the progenitor was a massive star it is possible that the total duration of the engine was longer than the rest-frame duration of 1 s, but somehow the jet could not emit gamma rays for a longer time. For example the jet could spend a longer time penetrating the envelope of the star. Alternatively, the jet might not be highly relativistic for longer than 1 s, so that no bright gamma rays could be produced after this time like, e.g., in the case of a newborn magnetar that initially injects a baryon-loaded, neutrino-driven wind (see also Ghisellini et al. 2020). Zhang et al. (2021) also noted that the energy injection from the newborn magnetar could explain the late shallow decay observed in the X-rays. Other alternatives exist like the mechanism known as the inhomogeneous jet model, proposed by Yamazaki et al. (2004), in which the jet consists of multiple subjets that we observe as SGRBs. Therefore, a fraction of SGRBs may come from collapsars. Peng et al. (2021) have recently proposed that the burst could have originated from the collapse of a Thorne–Żytkow–like object (TŻlO), which consists of a central NS and an envelope formed after a coalescence with a white dwarf. They found the collapse of such a TŻlO can naturally explain the short duration of GRB 200826A and the interaction between the disk wind and the ejected material can explain the "SN bump." However, this model needs to be proven with the updated photometry presented here, and in particular with our result that the SN is similar to those of other GRB-SNe. We have also demonstrated the importance of AO to studying GRBs. The NIR follow-up

observations presented here are the *first* to detect and pinpoint the location of an SN associated with a GRB, track the SN evolution, and determine the properties of the host galaxy. The last published attempts were more than 11 years ago and served only to provide information on the host galaxy of GRB 060418 (Pollack et al. 2009), and in the case of GRB 070610 to determine that an NIR transient was actually the counterpart of a galactic source (Castro-Tirado et al. 2008), making that GRB association uncertain (Kasliwal et al. 2008). The only other approach similar to the one outlined in this paper was the case of GRB 071003 (Perley et al. 2008). In that case, AO observations made it possible to detect the afterglow that was localized between two bright stars, but those observations were too early and the redshift too high to detect the associated SN ($\sim$16 days and $z = 1.60435$, respectively). The results presented here demonstrate clearly that AO can provide a powerful tool for studying GRBs.

5. Summary and Conclusions

GRB 200826A is a temporally short GRB at $z = 0.748577 \pm 0.000065$ with a rest-frame duration of $\sim$0.5 s, below the threshold of 2 s commonly used to separate SGRBs and LGRBs. To better understand the nature of this event, we initiated a follow-up campaign spanning a period of 1 yr that involved the LBT in Arizona (USA), the TNG telescope in La Palma (Canary Islands, Spain), and the MAO (Uzbekistan). Taking advantage of the AO capabilities of the LBT, we were able to obtain deep H-band observations between 37 and 159 days (observer-frame), corresponding to the rest-frame z' band at 21–91 days after the burst trigger. Image subtraction showed a faint transient within its host galaxy. Moreover, image subtraction of archival Gemini i'-band images with late reference observations obtained with the LBT revealed an optical transient that was less affected by oversubtraction than when reference images obtained at an earlier time after the GRB were used. Finally, we were able to put strong upper limits on the UV rest-frame luminosity thanks to our LBT and TNG r'-band observations. Our results show the following:

1. Despite its short duration, this event is consistent with the $E_{\rm p,i}$–$E_{\rm iso}$ "Amati" relation followed by LGRBs. The spectral lag is also more typical of LGRBs.
2. It was followed by a relatively faint optical and X-ray afterglow with a luminosity that lies between those of LGRB and SGRB afterglows.
3. The evolution and color of the late bump are in good agreement with other GRB-SNe, especially with the fast-rising GRB 130702A/SN 2013dx. GRB 200826A is among the cosmologically most remote GRB-SNe detected to date, close to the sensitivity limit of the present generation of 8–10 m class optical telescopes.
4. The possible alternative scenario of a genuine SGRB followed by a KN like AT 2017gfo is not supported by the different evolution and luminosity of the light curve of the observed transient.
5. The host galaxy of GRB 200826A is remarkable because it is typical of an LGRB host galaxy, but has a higher SFR and sSFR than expected.
6. The GRB lies at a projected distance of 0.75 kpc from the center of its host galaxy, which is consistent with the majority of LGRBs.

In summary, with the obtained results we are faced with a GRB of short duration that exploded in a star-forming galaxy, with a moderately faint afterglow, emitted by a jet most likely propagating into a wind environment, and followed by a bump in the light curve whose color and luminosity are typical of a GRB-SN. Thus we firmly classify this burst as a collapsar event. This evidence, together with the analysis of the energetics of this burst, further weakens the effectiveness of simple duration as an indicator of the source of a GRB. In addition, strong support is provided to theoretical predictions that collapsar-produced events may have an observable duration well short of the classical short/long divide (about 2 s), and down to 0.5 s or less (e.g., Bromberg et al. 2013).

In the following years future missions, like the Space Variable Objects Monitor (SVOM; Paul et al. 2011) and the Gamow Explorer (White et al. 2021), will offer a combination of extended sensitivity and energy bands, which will increase the number of known GRBs. This, when coupled with the improved capabilities of the new generation of extremely large telescopes, will allow us to observe both the GRB and SN components resulting from collapsar explosions in increasing numbers and at higher redshifts (e.g., Maiorano et al. 2018; Rossi et al. 2018). In this scenario, the first detection of an SN with AO observations represents what ground-based telescopes can achieve: they will not just offer a sharper view of the GRB-SN location within its host, but have the necessary depth to discover GRB-SNe at larger redshift than what has been possible up to now from the ground, and yet at similar wavelengths in the rest frame. Eventually, these future facilities will assess whether peculiar events like GRB 200826A are actually the result of the rich variety of collapsar phenomena (Amati 2021).

Ohio State University, representing OSU, University of Notre Dame, University of Minnesota, and University of Virginia. This work made use of data supplied by the UK Swift Science Data Centre at the University of Leicester.

Facilities: Swift, Fermi, Wind (Konus), LBT, TNG, Maidanak:1.5m.

Software: IRAF (Tody 1993), PyRAF (Science Software Branch at STScI 2012), DRAGONS (Labrie et al. 2019), HOTPANTS (Becker 2015), Le PHARE (Arnouts et al. 1999; Ilbert et al. 2006), WCSTools (Mink 2019).

Appendix
Spectral Lag

We first extracted the Fermi/GBM light curves with 1 ms resolution for the best exposed NaI detectors 6, 7, 8, 9, and 11 and calculated the corresponding total light curve in the same energy bands in Zhang et al. (2021): 10–20 keV, and 250–300 keV. We linearly interpolated the background counts of the 16 ms binned curves by fitting the time windows $[-10: -2] \cup [7:10]$ s.

For the spectral lag calculation, we then restricted the following analysis to the time interval $[-0.5:4]$ s and calculated the cross-correlation function (CCF) between the background-subtracted profiles of the two energy bands, using both the original binning of 1 ms and that of 16 ms. A positive lag corresponds to the softer band lagging behind the harder one. The peak of the CCF was found to be about 100 ms. To provide a more accurate estimate, we fitted the CCF around the peak with a third-degree polynomial between -0.4 and 0.6 s and it gave 95 ms. To estimate the uncertainty, we carried out the following simulations: starting from the 16 ms profiles, we obtained smooth versions of these curves by adopting the L1 trend filtering by Politsch et al. (2020) properly adapted to modeling GRB light curves (e.g., see Ghirlanda et al. 2021). We then obtained 1000 random realizations of both profiles by assuming uncorrelated Poisson noise, assuming the total expected count for each temporal bin (i.e., the interpolated background plus the smoothed GRB signal). For each pair of simulated profiles the corresponding CCF was fitted around the peak following the same procedure as that for the real CCF. We finally collected the resulting distribution of 1000 lags shown in Figure 11: this is approximately normal with a mean and standard deviation of (96 ± 38) ms, which therefore represents our estimate with uncertainty for the lag between the chosen energy bands. Our value looks slightly smaller than the analogous result by Zhang et al. (2021), who obtained (157 ± 51) ms, but it is statistically compatible and well in accord with the values obtained by those authors for adjacent energy bands (see their Extended Data Figure 4).

We finally repeated the same simulations using the 1 ms light curves, still adopting the same smoothed versions properly calibrated to 1 ms bins, and obtained a very similar result.

ORCID iDs

A. Rossi https://orcid.org/0000-0002-8860-6538
B. Rothberg https://orcid.org/0000-0003-2283-2185
E. Palazzi https://orcid.org/0000-0002-8691-7666
D. A. Kann https://orcid.org/0000-0003-2902-3583
L. Amati https://orcid.org/0000-0001-5355-7388
S. Klose https://orcid.org/0000-0001-8413-7917
A. Perego https://orcid.org/0000-0002-0936-8237
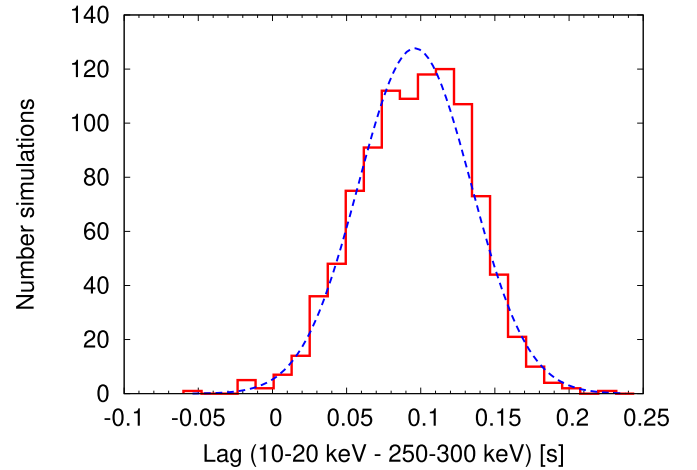
Figure 11. Distribution of the spectral lag analysis.

E. Pian https://orcid.org/0000-0001-8646-4858
C. Guidorzi https://orcid.org/0000-0001-6869-0835
A. S. Pozanenko https://orcid.org/0000-0001-9435-1327
G. Agapito https://orcid.org/0000-0002-6382-2613
S. Covino https://orcid.org/0000-0001-9078-5507
F. Cusano https://orcid.org/0000-0003-2910-6565
V. D'Elia https://orcid.org/0000-0002-7320-5862
M. Della Valle https://orcid.org/0000-0003-3142-5020
N. Masetti https://orcid.org/0000-0001-9487-7740
A. Melandri https://orcid.org/0000-0002-2810-2143
A. Nicuesa Guelbenzu https://orcid.org/0000-0002-6856-9813
D. Paris https://orcid.org/0000-0002-7409-8114
S. Paiano https://orcid.org/0000-0002-2239-3373
C. Plantet https://orcid.org/0000-0002-3898-4004
F. Rossi https://orcid.org/0000-0002-3544-1629
R. Salvaterra https://orcid.org/0000-0002-9393-8078
S. Schulze https://orcid.org/0000-0001-6797-1889
C. Veillet https://orcid.org/0000-0003-0272-0418

References

Abbott, B. P., Abbott, R., Abbott, T. D., et al. 2017a, ApJL, 848, L13
Abbott, B. P., Abbott, R., Abbott, T. D., et al. 2017b, ApJL, 848, L12
Abbott, B. P., Abbott, R., Abbott, T. D., et al. 2017c, PhRvL, 119, 161101
Agüí Fernández, J. F., Thöne, C. C., Kann, D. A., et al. 2021, arXiv:2109.13838
Ahumada, T., Anand, S., Sten, R., et al. 2020a, GCN, 28295, 1
Ahumada, T., Kumar, H., Fremling, C., et al. 2020b, GCN, 29029, 1
Ahumada, T., Singer, L., Kumar, H., et al. 2020c, GCN, 28727, 1
Ahumada, T., Singer, L. P., Anand, S., et al. 2021, NatAs, 5, 917
Alam, S., Albareti, F. D., Allende Prieto, C., et al. 2015, ApJS, 219, 12
Amati, L. 2006, MNRAS, 372, 233
Amati, L. 2021, NatAs, 5, 877
Amati, L., D'Agostino, R., Luongo, O., Muccino, M., & Tantalo, M. 2019, MNRAS, 486, L46
Amati, L., Frontera, F., Tavani, M., et al. 2002, A&A, 390, 81
Antonelli, L. A., D'Avanzo, P., Perna, R., et al. 2009, A&A, 507, L45
Arnouts, S., Cristiani, S., Moscardini, L., et al. 1999, MNRAS, 310, 540
Ascenzi, S., Coughlin, M. W., Dietrich, T., et al. 2019, MNRAS, 486, 672
Ashall, C., Mazzali, P. A., Pian, E., et al. 2019, MNRAS, 487, 5824
Barbieri, C., Salafia, O. S., Perego, A., Colpi, M., & Ghirlanda, G. 2019, A&A, 625, A152
Barthelmy, S., Barbier, L., Cummings, J., et al. 2006, GCN, 5256, 1
Becker, A. 2015, HOTPANTS: High Order Transform of PSF ANd Template Subtraction, Astrophysics Source Code Library, ascl:1504.004
Belkin, S., Zhornichenko, A., Pozanenko, A., et al. 2020a, GCN, 28306, 1
Belkin, S. O., Pozanenko, A. S., Mazaeva, E. D., et al. 2020b, AstL, 46, 783
Bellm, E. C., Kulkarni, S. R., Barlow, T., et al. 2019, PASP, 131, 068003

Bellstedt, S., Robotham, A. S. G., Driver, S. P., et al. 2021, MNRAS, 503, 3309

Bernuzzi, S., Breschi, M., Daszuta, B., et al. 2020, MNRAS, 497, 1488

Beuermann, K., Hessman, F. V., Reinsch, K., et al. 1999, A&A, 352, L26

Bian, F., Kewley, L. J., & Dopita, M. A. 2018, ApJ, 859, 175

Blanchard, P. K., Berger, E., & Fong, W.-F. 2016, ApJ, 817, 144

Bloom, J. S., Kulkarni, S. R., & Djorgovski, S. G. 2002, AJ, 123, 1111

Bromberg, O., Nakar, E., Piran, T., & Sari, R. 2012, ApJ, 749, 110

Bromberg, O., Nakar, E., Piran, T., & Sari, R. 2013, ApJ, 764, 179

Cano, Z., Wang, S.-Q., Dai, Z.-G., & Wu, X.-F. 2017a, AdAst, 2017, 8929054

Cano, Z., Izzo, L., de Ugarte Postigo, A., et al. 2017b, A&A, 605, A107

Cardelli, J. A., Clayton, G. C., & Mathis, J. S. 1989, ApJ, 345, 245

Castro-Tirado, A. J., de Ugarte Postigo, A., Gorosabel, J., et al. 2008, Natur, 455, 506

Christensen, L., Vergani, S. D., Schulze, S., et al. 2017, A&A, 608, A84

Curti, M., Cresci, G., Mannucci, F., et al. 2017, MNRAS, 465, 1384

D'Ai, A., Sbarufatti, B., Oates, S. R., et al. 2020, GCN, 28300, 1

Dainotti, M. G., Livermore, S., Kann, D. A., et al. 2020, ApJL, 905, L26

D'Avanzo, P., Salvaterra, R., Bernardini, M. G., et al. 2014, MNRAS, 442, 2342

de Ugarte Postigo, A., Horváth, I., Veres, P., et al. 2011, A&A, 525, A109

D'Elia, V., Pian, E., Melandri, A., et al. 2015, A&A, 577, A116

Della Valle, M., Malesani, D., Bloom, J. S., et al. 2006, ApJL, 642, L103

Dichiara, S., Cenko, S. B., Troja, E., et al. 2020, GCN, 28312, 1

Evans, P. A., Willingale, R., Osborne, J. P., et al. 2010, A&A, 519, A102

Ferrero, P., Kann, D. A., Zeh, A., et al. 2006, A&A, 457, 857

Fong, W., Laskar, T., Rastinejad, J., et al. 2021, ApJ, 906, 127

Fontana, A., Dunlop, J. S., Paris, D., et al. 2014, A&A, 570, A11

Fynbo, J. P. U., Watson, D., Thöne, C. C., et al. 2006, Natur, 444, 1047

Gaia Collaboration, Brown, A. G. A., Vallenari, A., et al. 2018, A&A, 616, A1

Gal-Yam, A., Fox, D. B., Price, P. A., et al. 2006, Natur, 444, 1053

Galama, T. J., Vreeswijk, P. M., van Paradijs, J., et al. 1998, Natur, 395, 670

Gao, H., Zhang, B., Lü, H.-J., & Li, Y. 2017, ApJ, 837, 50

Gehrels, N., Barthelmy, S. D., Burrows, D. N., et al. 2008, ApJ, 689, 1161

Ghirlanda, G., Salvaterra, R., Toffano, M., et al. 2021, ExA, 52, 277

Ghisellini, G., Ghirlanda, G., Oganesyan, G., et al. 2020, A&A, 636, A82

Giallongo, E., Ragazzoni, R., Grazian, A., et al. 2008, A&A, 482, 349

Gompertz, B. P., Levan, A. J., Tanvir, N. R., et al. 2018, ApJ, 860, 62

González-Gaitán, S., Tominaga, N., Molina, J., et al. 2015, MNRAS, 451, 2212

Granot, J., & Sari, R. 2002, ApJ, 568, 820

Greiner, J., Krühler, T., Fynbo, J. P. U., et al. 2009, ApJ, 693, 1610

Greiner, J., Mazzali, P. A., Kann, D. A., et al. 2015, Natur, 523, 189

Gupta, S., Sharma, V., Vibhute, A., et al. 2020, GCN, 28288, 1

Hamburg, R., Malacaria, C., Meegan, C. & Fermi GBM Team 2020, GCN, 29140, 1

Horváth, I., & Tóth, B. G. 2016, Ap&SS, 361, 155

Hu, Y. D., Castro-Tirado, A. J., Kumar, A., et al. 2021, A&A, 646, A50

Huang, K. Y., Urata, Y., Filippenko, A. V., et al. 2005, ApJL, 628, L93

Hullinger, D., Barbier, L., Barthelmy, S., et al. 2006, 5142, 1

Hunt, L. K., Palazzi, E., Michałowski, M. J., et al. 2014, A&A, 565, A112

Hurley, K., Mitrofanov, I. G., Golovin, D., et al. 2020, GCN, 28291, 1

Ilbert, O., Arnouts, S., McCracken, H. J., et al. 2006, A&A, 457, 841

Im, M., Ko, J., Cho, Y., et al. 2010, JKAS, 43, 75

Izzo, L., de Ugarte Postigo, A., Maeda, K., et al. 2019, Natur, 565, 324

Jakobsson, P., Hjorth, J., Fynbo, J. P. U., et al. 2004, ApJL, 617, L21

Japelj, J., Vergani, S. D., Salvaterra, R., et al. 2016, A&A, 590, A129

Jin, Z.-P., Li, X., Cano, Z., et al. 2015, ApJL, 811, L22

Jin, Z.-P., Zhou, H., Covino, S., et al. 2021, arXiv:2109.07694

Kann, D. A., Klose, S., & Zeh, A. 2006, ApJ, 641, 993

Kann, D. A., Oates, S. R., Rossi, A., et al. 2021, arXiv:2110.00110

Kann, D. A., Klose, S., Zhang, B., et al. 2010, ApJ, 720, 1513

Kann, D. A., Klose, S., Zhang, B., et al. 2011, ApJ, 734, 96

Kann, D. A., Schady, P., Olivares, E. F., et al. 2019, A&A, 624, A143

Kasliwal, M. M., Cenko, S. B., Kulkarni, S. R., et al. 2008, ApJ, 678, 1127

Kawaguchi, K., Shibata, M., & Tanaka, M. 2020, ApJ, 889, 171

Kelly, P. L., Filippenko, A. V., Modjaz, M., & Kocevski, D. 2014, ApJ, 789, 23

Kennicutt, R. C. J. 1998, ARA&A, 36, 189

Klose, S., Schmidl, S., Kann, D. A., et al. 2019, A&A, 622, A138

Korobkin, O., Wollaeger, R. T., Fryer, C. L., et al. 2021, ApJ, 910, 116

Kouveliotou, C., Meegan, C. A., Fishman, G. J., et al. 1993, ApJL, 413, L101

Krimm, H. A., Barthelmy, S. D., Laha, S., et al. 2020, GCN, 29139, 1

Labrie, K., Anderson, K., Cárdenes, R., Simpson, C., & Turner, J. E. H. 2019, in ASP Conf. Ser. 523, Astronomical Data Analysis Systems and Systems XXVII, ed. P. J. Teuben et al. (San Francisco, CA: ASP), 321

Lamareille, F. 2010, A&A, 509, A53

Maiolino, R., & Mannucci, F. 2019, A&ARv, 27, 3

Maiorano, E., Amati, L., Rossi, A., et al. 2018, MmSAI, 89, 181

Mangan, J., Dunwoody, R., Meegan, C. & Fermi GBM Team 2020, GCN, 28287, 1

Marocco, J., Hache, E., & Lamareille, F. 2011, A&A, 531, A71

Mazets, E. P., Golenetskii, S. V., Ilinskii, V. N., et al. 1981, Ap&SS, 80, 3

Mazzali, P. A., Pian, E., Bufano, F., & Ashall, C. 2021, MNRAS, 505, 4106

McBreen, S., Foley, S., Watson, D., et al. 2008, ApJL, 677, L85

Melandri, A., Malesani, D. B., Izzo, L., et al. 2019, MNRAS, 490, 5366

Melandri, A., Izzo, L., Pian, E., et al. 2022, A&A, 659, A39

Metzger, B. D., & Piro, A. L. 2014, MNRAS, 439, 3916

Michałowski, M. J., Xu, D., Stevens, J., et al. 2018, A&A, 616, A169

Minaev, P. Y., & Pozanenko, A. S. 2020a, MNRAS, 492, 1919

Minaev, P. Y., & Pozanenko, A. S. 2020b, AstL, 46, 573

Mink, J. 2019, in ASP Conf. Ser. 523, Astronomical Data Analysis Software and Systems XXVII, ed. P. J. Teuben (San Francisco, CA: ASP), 281

Modjaz, M., Bianco, F. B., Siwek, M., et al. 2020, ApJ, 892, 153

Nicuesa Guelbenzu, A., Klose, S., Rossi, A., et al. 2011, A&A, 531, L6

Nicuesa Guelbenzu, A., Klose, S., Greiner, J., et al. 2012, A&A, 548, A101

Norris, J. P., Nemiroff, R. J., Bonnell, J. T., et al. 1996, ApJ, 459, 393

Nysewander, M., Fruchter, A. S., & Pe'er, A. 2009, ApJ, 701, 824

O'Connor, B., Troja, E., Dichiara, S., et al. 2021, MNRAS, 502, 1279

Ofek, E. O., Cenko, S. B., Gal-Yam, A., et al. 2007, ApJ, 662, 1129

Olivares, E. F., Greiner, F., Schady, J., et al. 2012, A&A, 539, A76

Osterbrock, D. E. 1989, Astrophysics of Gaseous Nebulae and Active Galactic Nuclei (Mill Valley, CA: Univ. Science Books)

Paul, J., Wei, J., Basa, S., & Zhang, S.-N. 2011, CRPhy, 12, 298

Pei, Y. C. 1992, ApJ, 395, 130

Peng, Z.-K., Liu, Z.-K., & Zhang, B.-B. 2021, arXiv:2109.06041

Perego, A., Radice, D., & Bernuzzi, S. 2017, ApJL, 850, L37

Perley, D. A., Li, W., Chornock, R., et al. 2008, ApJ, 688, 470

Perley, D. A., Levan, A. J., Tanvir, N. R., et al. 2013, ApJ, 778, 128

Pian, E., D'Avanzo, P., Benetti, S., et al. 2017, Natur, 551, 67

Pinna, E., Rossi, F., Puglisi, A., et al. 2021, arXiv:2101.07091

Pittori, C., Verrecchia, F., Ursi, A., et al. 2020, GCN, 28289, 1

Planck Collaboration, Ade, P. A. R., Aghanim, N., et al. 2016, A&A, 594, A13

Pogge, R. W., Atwood, B., Brewer, D. F., et al. 2010, Proc. SPIE, 7735, 77350A

Politsch, C. A., Cisewski-Kehe, J., Croft, R. A. C., & Wasserman, L. 2020, MNRAS, 492, 4005

Pollack, L. K., Chen, H. W., Prochaska, J. X., & Bloom, J. S. 2009, ApJ, 701, 1605

Radice, D., Perego, A., Bernuzzi, S., & Zhang, B. 2018a, MNRAS, 481, 3670

Radice, D., Perego, A., Hotokezaka, K., et al. 2018b, ApJ, 869, 130

Rastinejad, J. C., Fong, W., Kilpatrick, C. D., et al. 2021, ApJ, 916, 89

Rhodes, L., Fender, R., Williams, D. R. A., & Mooley, K. 2021, MNRAS, 503, 2966

Ridnaia, A., Golenetskii, S., Aptekar, R., et al. 2020, GCN, 28294, 1

Rossi, A., Stratta, G., Maiorano, E., et al. 2018, MmSAI, 89, 254

Rossi, A., Klose, S., Ferrero, P., et al. 2012, A&A, 545, A77

Rossi, A., D'Avanzo, P., D'Elia, V., et al. 2020a, GCN, 28949, 1

Rossi, A., Stratta, G., Maiorano, E., et al. 2020b, MNRAS, 493, 3379

Rothberg, B., Kuhn, O., Veillet, C., & Allanson, S. 2020a, GCN, 28319, 1

Rothberg, B., Power, J., Kuhn, O., et al. 2020b, Proc. SPIE, 11447, 1144706

Sagues Carracedo, A., Kumar, H., Ahumada, T., et al. 2020, GCN, 28293, 1

Sari, R., Piran, T., & Narayan, R. 1998, ApJL, 497, L17

Savaglio, S., Glazebrook, K., & Le Borgne, D. 2009, ApJ, 691, 182

Schlafly, E. F., & Finkbeiner, D. P. 2011, ApJ, 737, 103

Schreiber, C., Elbaz, D., Pannella, M., et al. 2018, A&A, 609, A30

Schulze, S., Klose, S., Björnsson, G., et al. 2011, A&A, 526, A23

Schulze, S., Malesani, D., Cucchiara, A., et al. 2014, A&A, 566, A102

Schulze, S., Krühler, T., Leloudas, G., et al. 2018, MNRAS, 473, 1258

Science Software Branch at STScI 2012, PyRAF: Python alternative for IRAF, Astrophysics Source Code Library, ascl:1207.011

Seifert, W., Appenzeller, I., Baumeister, H., et al. 2003, Proc. SPIE, 4841, 962

Siegel, D. M., & Ciolfi, R. 2016, ApJ, 819, 14

Skrutskie, M. F., Cutri, R. M., Stiening, R., et al. 2006, AJ, 131, 1163

Smartt, S. J., Chen, T.-W., Jerkstrand, A., et al. 2017, Natur, 551, 75

Soderberg, A. M., Kulkarni, S. R., Price, P. A., et al. 2006, ApJ, 636, 391

Svinkin, D., Frederiks, D., Ridnaia, A., Tsvetkova, A. & Konus-Wind Team 2020, GCN, 28301, 1

Tanga, M., Krühler, T., Schady, P., et al. 2018, A&A, 615, A136

Thöne, C. C., Campana, S., Lazzati, D., et al. 2011, MNRAS, 414, 479

Tody, D. 1993, in ASP Conf. Ser. 52, Astronomical Data Analysis Software and Systems II, ed. R. J. Hanisch, R. J. V. Brissenden, & J. Barnes (San Francisco, CA: ASP), 173

Toy, V. L., Cenko, S. B., Silverman, J. M., et al. 2016, ApJ, 818, 79

Trouille, L., Barger, A. J., & Tremonti, C. 2011, ApJ, 742, 46

Vergani, S. D., Petitjean, P., Ledoux, C., et al. 2009, A&A, 503, 771

Vergani, S. D., Salvaterra, R., Japelj, J., et al. 2015, A&A, 581, A102

Volnova, A. A., Pruzhinskaya, M. V., Pozanenko, A. S., et al. 2017, MNRAS, 467, 3500

White, N. E., Bauer, F. E., Baumgartner, W., et al. 2021, Proc. SPIE, 11821, 1182109

Wiersema, K., van der Horst, A. J., Kann, D. A., et al. 2008, A&A, 481, 319

Willingale, R., Starling, R. L. C., Beardmore, A. P., Tanvir, N. R., & O'Brien, P. T. 2013, MNRAS, 431, 394

Woosley, S. E., & Bloom, J. S. 2006, ARA&A, 44, 507

Xu, D., Starling, R. L. C., Fynbo, J. P. U., et al. 2009, ApJ, 696, 971

Yamazaki, R., Ioka, K., & Nakamura, T. 2004, ApJL, 607, L103

Yang, B., Jin, Z.-P., Li, X., et al. 2015, NatCo, 6, 7323

Yu, Y.-W., Zhang, B., & Gao, H. 2013, ApJL, 776, L40

Zeh, A., Klose, S., & Hartmann, D. H. 2004, ApJ, 609, 952

Zeh, A., Klose, S., & Kann, D. A. 2006, ApJ, 637, 889

Zhang, B., Zhang, B.-B., Virgili, F. J., et al. 2009, ApJ, 703, 1696

Zhang, B. B., Liu, Z. K., Peng, Z. K., et al. 2021, NatAs, 5, 911

Zhu, J.-P., Yang, Y.-P., Liu, L.-D., et al. 2020, ApJ, 897, 20